https://doi.org/10.5194/egusphere-2024-872
Preprint. Discussion started: 10 April 2024

Present-Day Methane Shortwave Absorption Mutes Surface Warming and Wetting Relative to Preindustrial Conditions

Robert J. Allen[1], Xueying Zhao[1,2,3], Cynthia A. Randles[4*], Ryan J. Kramer[5], Bjørn H. Samset[6] and Christopher J. Smith[7,8]

[1]Department of Earth and Planetary Sciences, University of California, Riverside, CA, USA.

[2]National Center for Atmospheric Research, Boulder, CO.

[3]Department of Earth and Planetary Science, The University of Texas at Austin, Austin, TX, USA.

[4]ExxonMobil Technology and Engineering Company, Annandale, NJ, USA
[*]now at UNEP International Methane Emission Observatory, Paris, France.

[5]NOAA Geophysical Fluid Dynamics Laboratory, Princeton, NJ.

[6]CICERO Center for International Climate and Environmental Research in Oslo, Oslo, Norway.

[7]School of Earth and Environment, University of Leeds, Leeds, UK.

[8]International Institute for Applied Systems Analysis (IIASA), Laxenburg, Austria.

Correspondence to: Robert J. Allen (rjallen@ucr.edu)

Short Summary:

Present-day methane shortwave absorption mutes 29% of the surface warming and 66% of the precipitation increase associated with its longwave absorption. The muting effect of present-day methane shortwave absorption is about five times larger as compared to that under idealized carbon dioxide perturbations.

https://doi.org/10.5194/egusphere-2024-872
Preprint. Discussion started: 10 April 2024

Abstract. Recent analyses show the importance of methane shortwave absorption, which many climate models lack. In particular, Allen et al. (2023) used idealized climate model simulations to show that methane shortwave absorption mutes up to 30% of the surface warming and 60% of the precipitation increase associated with its longwave radiative effects. Here, we explicitly quantify the radiative and climate impacts due to shortwave absorption of the present-day methane perturbation using the Community Earth System Model version 2 (CESM2). Our results corroborate that present-day methane shortwave absorption mutes the warming and wetting effects of longwave absorption. For example, the global mean cooling in response to the present-day methane shortwave absorption is -0.10$\pm$0.04 K, which offsets 29% of the surface warming associated with present-day methane longwave radiative effects. Similarly, we explicitly estimate 66% of the precipitation increase associated with the longwave radiative effects of the present-day methane perturbation is offset by shortwave absorption. Unlike other solar absorbers (i.e., black carbon), the decrease in global mean precipitation under methane shortwave absorption is driven by both fast (atmospheric absorption) and slow (surface temperature cooling) responses. Finally, we show that the present-day methane shortwave radiative effects, relative to its longwave radiative effects, are about five times larger as compared to those under idealized carbon dioxide perturbations. The unique responses to methane shortwave absorption are related to its vertical atmospheric solar heating profile. Methane remains a potent greenhouse gas and continued endeavors to decrease methane emissions are necessary to stay below the 1.5°C global warming threshold.

https://doi.org/10.5194/egusphere-2024-872
Preprint. Discussion started: 10 April 2024

1 Introduction

Several recent studies (Li et al., 2010; Etiminan et al., 2016; Collins et al., 2018; Byrom and Shine, 2022) have shown the significance of methane (CH_4) shortwave (SW) absorption—which is lacking in many climate models (Forster et al., 2021)—at near-infrared (NIR) wavelengths. Etminan et al. (2016) first showed methane SW absorption increases its stratospherically adjusted radiative forcing (SARF) by up to ~15% as compared to its longwave (LW) SARF. Smith et al. (2018) subsequently inferred negative rapid adjustments (i.e., surface temperature independent responses) due to CH_4 SW absorption, using four of ten models from the Precipitation Driver and Response Model Intercomparison Project (PDRMIP; Myhre et al., 2017) that included an explicit representation of methane SW absorption. Byrom and Shine (2022) showed that CH_4 SW forcing depends on several factors, including the spectral variation of surface albedo, the vertical profile of methane, and absorption of solar radiation at longer wavelengths, specifically methane's 7.6 µm band. They estimated a smaller impact of CH_4 SW absorption, with a 7% increase in SARF, in part due to the inclusion of the 7.6 µm band which mainly impacts stratospheric solar absorption.

The recent analysis of Allen et al. (2023) (hereafter referred to as A23) used Community Earth System Model version 2 (CESM2; Danabasoglu et al., 2020) simulations to isolate CH_4 SW absorption, and showed that it muted the surface warming and wetting due to methane's LW radiative effects. Muting of surface warming was attributed largely to cloud rapid adjustments, including increased low-level clouds and decreased high-level clouds. These cloud changes in turn were associated with the vertical profile of atmospheric solar heating, and corresponding changes to atmospheric temperature and relative humidity.

We adopt similar terminology as in A23. Throughout this manuscript, the terms "SW radiative effect"/"SW absorption" and "LW radiative effect" refers to the radiative effects of methane (and eventually carbon dioxide) on the climate system as isolated by a suite of simulations (to be discussed below). This terminology is used interchangeably with the abbreviations "CH_{4SW}" and "CH_{4LW}", respectively.

A23 focused on three idealized methane perturbations, including 2x, 5x and 10x preindustrial methane concentrations. Relatively large perturbations were emphasized to maximize the signal to noise ratio, as well as to robustly identify mechanisms. Despite these relatively large methane perturbations, 5x preindustrial methane concentrations are comparable to end of 21st century projections under the

https://doi.org/10.5194/egusphere-2024-872
Preprint. Discussion started: 10 April 2024

Shared Socioeconomic Pathway 3-7.0 (i.e., 0.75 ppm to 3.4 ppm). Although $5xCH_4$ and $10xCH_4$ SW radiative effects showed a clear muting of the corresponding LW effects, $2xCH_4$ did not. For example, the global mean near-surface air temperature (TAS) response under $5xCH_{4SW}$ and $10xCH_{4SW}$ (Figure 1a) yielded significant global cooling at -0.23 and -0.39 K. $2xCH_{4SW}$, however, yielded a warming response of 0.06 K that was not significant at the 90% confidence level. Similar results apply for the global mean precipitation (PRECIP) response (Figure 1b), where a significant decrease occurred under $5xCH_{4SW}$ and $10xCH_{4SW}$ at -0.021 and -0.039 mm d^{-1} (-0.7 and -1.3%). For $2xCH_{4SW}$, the response was again not significant at 0.0018 mm d^{-1} (0.06%). The lack of significant climate responses in the $2xCH_{4SW}$ coupled ocean-atmosphere simulation is consistent with its relatively weak forcing as compared to the larger methane perturbations, and relative to internal climate variability of the coupled ocean-atmosphere system.

A23 subsequently inferred the present-day methane effects from linear regression applied to the 2x, 5x, and $10xCH_4$ perturbations (dashed lines in Figure 1a,b). Their inferred estimate of the present-day (assumed to be $2.4xCH_4$) effect of CH_4 SW absorption on global mean TAS and PRECIP were consistent with the overall conclusions, with cooling of -0.04 K and a decrease in precipitation of -0.15%. However, these CH_{4SW} responses represent muting of the corresponding CH_{4LW} responses of only 18% and 50%, respectively, which are much lower than the muting under the larger methane perturbations at ~30% for TAS and ~60% for PRECIP.

Given the caveats of the above approach (i.e., the assumption of linearity), here we conduct analogous simulations as A23 to explicitly calculate the shortwave absorption effects of the present-day methane concentration, i.e., the ~750 to ~1900 ppb increase (~2.5x). Our results corroborate the prior, inferred estimate from A23, while also indicating that the muting of warming and wetting due to present-day methane shortwave absorption was underestimated. We further expand upon our understanding of the climate effects of CH_{4SW} by conducting an atmospheric energy budget analysis, and by comparing the effects of methane SW absorption with those from carbon dioxide SW absorption.

2 Materials and Methods

An array of targeted methane-only equilibrium climate simulations are conducted with CESM2 (Danabasoglu et al., 2020), which includes the most recent model components such as the Community Atmosphere Model version 6 (CAM6).

https://doi.org/10.5194/egusphere-2024-872
Preprint. Discussion started: 10 April 2024

CAM6's radiation parameterization, the Rapid Radiative Transfer Model for general circulation models (RRTMG; Iacono et al., 2008) includes a representation of CH_4 SW absorption in three near-infrared bands including 1.6-1.9 μm, 2.15-2.50 μm and 3.10-3.85 μm. Methane shortwave absorption at 7.6 μm (the mid-infrared; mid-IR), however, is not represented. Furthermore, although CESM2 includes a representation of CH_4 SW absorption, RRTMG underestimates CH_4 (and CO_2) SW IRF by 25-45% (Hogan and Matricardi, 2020).

Our focus here is a set of 2.5x preindustrial atmospheric CH_4 concentration simulations, to complement the three methane perturbations (2x, 5x and 10x preindustrial atmospheric CH_4 concentrations) performed by A23. We perform both fixed climatological sea surface temperatures (fSST) and fully coupled ocean-atmosphere simulations (Table 1), and conduct two sets of identical experiments, one that includes CH_4 LW+SW radiative effects ($2.5xCH_4^{EXP}$) and one that lacks CH_4 SW radiative effects ($2.5xCH_{4NOSW}^{EXP}$). CH_4 SW absorption in the three NIR bands in RRTMG is turned off in the simulations that lack methane SW absorption. These are compared to a default preindustrial control experiment (PIC^{EXP}), which includes CH_4 (as well as other radiative species such as CO_2) LW+SW radiative effects, as well as to a preindustrial control experiment with CH_4 SW radiative effects turned off (i.e., LW effects only, denoted as $PIC_{NOCH4SW}^{EXP}$). To clarify, SW changes can still be present in $2.5xCH_{4NOSW}^{EXP}$, but only as an adjustment (or feedback) associated with the direct LW absorption of methane. For example, direct LW absorption of methane can drive changes in water vapor and clouds, which in turn could impact SW radiation.

This suite of CH_4 simulations allows quantification of the CH_4 LW+SW, LW and SW radiative effects, denoted as $2.5xCH_{4LW+SW}$, $2.5xCH_{4LW}$ and $2.5xCH_{4SW}$. The $2.5xCH_{4LW+SW}$ signal is obtained by subtracting the default $2.5xCH_4$ perturbation from the default control ($2.5xCH_4^{EXP} - PIC^{EXP}$). The $2.5xCH_{4LW}$ signal is obtained by subtracting the $2.5xCH_4$ perturbation without CH_4 SW absorption from the corresponding control simulation without CH_4 SW absorption ($2.5xCH_{4NOSW}^{EXP} - PIC_{NOCH4SW}^{EXP}$). The $2.5xCH_{4SW}$ signal is obtained by taking the double difference, i.e., $(2.5xCH_4^{EXP} - PIC^{EXP}) - (2.5xCH_{4NOSW}^{EXP} - PIC_{NOCH4SW}^{EXP})$. The $2.5xCH_{4SW}$ signal therefore represents CH_4 SW absorption and also the impacts of this SW absorption on CH_4 LW adjustments (and feedbacks). We also calculate the corresponding instantaneous radiative forcing (IRF), which is defined as the initial perturbation to the radiation balance, using the Parallel Offline Radiative Transfer (PORT) model (Conley et al., 2013). PORT isolates the RRTMG radiative transfer computation from the CESM2-CAM6 model configuration.

https://doi.org/10.5194/egusphere-2024-872
Preprint. Discussion started: 10 April 2024

Fixed SST experiments are used to estimate the 'fast' climate responses and the effective radiative forcing (ERF). ERF is defined as the top-of-the-atmosphere (TOA) net radiative flux difference between the experiment and control simulation, with climatological fixed SSTs and sea-ice distributions without any adjustments for changes in the surface temperature over land (Forster et al., 2016). ERF can be decomposed into the sum of the IRF and rapid adjustments (ADJs). Rapid adjustments represent the change in state in response to the initial perturbation (i.e., IRF) excluding any responses related to changes in sea surface temperatures. The total climate response, which includes the IRF, ADJs and the surface temperature feedbacks, is quantified using the coupled ocean-atmosphere experiments. The surface temperature feedbacks (i.e., 'slow' response) are estimated as the difference between the coupled ocean atmosphere simulations and the climatologically fixed SST experiments. The rapid adjustments, which for example include clouds and water vapor, are estimated using the radiative kernel method (Soden et al., 2008; Smith et al., 2018, 2020) applied to the climatological fixed SST simulations. A radiative kernel is basically the partial derivative of the radiative flux with respect to a variable (e.g., moisture) that changes with temperature. It therefore represents the radiative impacts from small perturbations in a state. To calculate the rapid adjustments, the radiative kernel is multiplied by the change in the climate variable under consideration (from the fSST simulations). The Python-based radiative kernel toolkit of Soden et al. (2008), along with the Geophysical Fluid Dynamics Laboratory radiative kernel, are used here. The method for calculating cloud rapid adjustments with radiative kernels is a bit more involved. Here, we use the kernel difference method (Smith et al., 2018) which employs a cloud-masking correction applied to the cloud radiative-forcing diagnostics. The cloud-masking correction is based on the kernel-derived non-cloud adjustments and IRF. A23 showed that this methodology performed well, including a small residual term (i.e., $ERF - IRF - \Sigma ADJs < \sim 5\%$). Furthermore, similar results were obtained with an alternative radiative kernel based on CloudSat/CALIPSO (Kramer et al., 2019).

Our simulations are performed at 1.9° x 2.5° latitude-longitude resolution with 32 atmospheric levels. Coupled ocean-atmosphere experiments are initialized from a spun-up preindustrial control simulation and subsequently integrated for 90 years. Total climate responses are estimated using the last 40 years of these coupled ocean-atmosphere experiments. As climatologically fixed SST simulations equilibrate more quickly, these are run for 32 years. The ERF and rapid adjustments are estimated from the last 30 years of these fSST experiments.

A two-tailed pooled *t* test is used to assess the statistical significance of a climate

https://doi.org/10.5194/egusphere-2024-872
Preprint. Discussion started: 10 April 2024

response, based on the annual mean difference between the experiment and control. We evaluate a null hypothesis of zero difference with $n_1 + n_2 - 2$ degrees of freedom. Here, n_1 and n_2 are the number of years in the experiment and control simulations (e.g., 90 years for the coupled ocean-atmosphere runs). The pooled variance $\frac{(n1-1)S_1^2+(n2-1)S_2^2}{n1+n2-2}$ is used, where S_1 and S_2 are the sample variances.

3 Results

3.1 2.5xCH_4 Radiative Flux Components & Rapid Adjustments

Figure 2a shows the 2.5xCH_4 TOA ERF, IRF and ADJ, as well as the radiative kernel decomposition of ADJ (Fig. 2b). Corresponding plots for 2xCH_4 are also included in Fig. 2c,d. As expected, the 2.5xCH_4 produces a larger TOA IRF than 2xCH_4. For example, the TOA LW IRF increases from 0.32 W m^{-2} under 2xCH_4 (Fig. 2c) to 0.46 W m^{-2} under 2.5xCH_4 (Fig. 2a). The TOA SW IRF under 2.5xCH_4 is 0.06 W m^{-2} (Fig. 2a). Although this remains relatively small (and not statistically significant at the 90% confidence level), it represents a 50% increase relative to 2xCH_4 at 0.04 W m^{-2} (Fig. 2c).

Similarly, the 2.5xCH_4 instantaneous shortwave heating rate (QRS) profile (Figure 3a) exhibits slightly larger positive values as compared to 2xCH_4 for atmospheric pressure levels less than ~700 hPa. 2.5xCH_{4SW} also exhibits slightly larger negative QRS for pressure levels greater than ~700 hPa. As discussed in A23, increasing the atmospheric methane concentration does not increase lower-tropospheric SW heating because the three near-infrared bands are already highly saturated here (e.g., due to water vapor absorption). Furthermore, the methane-induced QRS increase aloft decreases the available solar radiation in the three near-IR methane absorption bands (1.6-1.9 μm, 2.15-2.50 μm and 3.10-3.85 μm) that can be absorbed by other gases (e.g., water vapor) in the lower-troposphere. This results in the decrease in SW heating-rate in the lower troposphere (Fig. 3a). Both of these features exist under 2.5xCH_{4SW} and are consistent with the larger methane perturbations (e.g., 5xCH_{4SW}), which feature relatively large QRS increases aloft and QRS decreases in the lower troposphere.

As mentioned above, A23 showed that methane SW radiative effects lead to a negative rapid adjustment (largely due to changes in clouds) that acts to cool the climate system. A positive ADJ represents a net energy increase, whereas a negative ADJ represents a net energy decrease. Individual rapid adjustments, as

https://doi.org/10.5194/egusphere-2024-872
Preprint. Discussion started: 10 April 2024

well as the total adjustment, under 2.5xCH_4 are displayed in Figure 2b. Under 2.5xCH_{4SW}, the total rapid adjustment is -0.16 W m^{-2}, which is largely due to the cloud adjustment at -0.12 W m^{-2}. The stratospheric temperature adjustment contributes the remainder at -0.04 W m^{-2}. The other components are relatively small and not significant at the 90% confidence level. Qualitatively similar but weaker (and not significant at the 90% confidence level) results occur for 2xCH_{4SW} (Fig. 2d). Thus, similar to the larger CH_4 perturbations in A23, 2.5xCH_{4SW} yields a significant negative total rapid adjustment that is largely due to the cloud adjustment.

This negative rapid adjustment promotes a negative ERF under methane SW absorption. This is because the ERF is the sum of ADJs and IRF. For example, under the larger 5xCH_{4SW} perturbation in A23, the ERF and ADJ were both significant at -0.22 W m^{-2} and -0.36 W m^{-2}, respectively. The corresponding ERF and ADJ for 2xCH_{4SW} (Fig. 2c) are also negative, but smaller in magnitude (and not significant at the 90% confidence level) at -0.09 and -0.13 W m^{-2}, respectively. Under 2.5xCH_{4SW}, the ERF and ADJ (Fig. 2a) are larger at -0.10 W m^{-2} and -0.16 W m^{-2}, respectively, with the latter significant at the 90% confidence level. As with the larger methane perturbations, 2.5xCH_{4SW} offsets ~20% of the ERF associated with 2.5xCH_{4LW} (0.53 W m^{-2}).

The corresponding surface CH_{4SW} "ERFs" (not shown) are more negative than those at the TOA, at -0.14 W m^{-2} for 2xCH_{4SW} and -0.18 W m^{-2} for 2.5xCH_{4SW} (the latter is significant at the 95% confidence interval). We note that technically this is not an ERF, but we retain this terminology since it is calculated analogously to ERF, just using surface as opposed to TOA radiative fluxes. This negative surface ERF is consistent with negative surface CH_{4SW} IRF values (due to atmospheric solar absorption, which decreases surface solar radiation), and the vertical redistribution of shortwave heating (Fig. 3a) that drives a negative surface rapid adjustment that is again largely due to the cloud adjustment. The surface CH_{4SW} IRF values are -0.07 W m^{-2} for 2xCH_{4SW} and -0.10 W m^{-2} for 2.5xCH_{4SW}, and the corresponding sum of the surface rapid adjustments are -0.07 W m^{-2} for 2xCH_{4SW} and -0.09 W m^{-2} for 2.5xCH_{4SW} (not shown).

To summarize, relative to 2xCH_{4SW}, 2.5xCH_{4SW} yields larger (10-20%) and more negative TOA and surface IRFs, ERFs, and ADJs. The larger negative ERFs (and ADJs) act to promote cooling.

https://doi.org/10.5194/egusphere-2024-872
Preprint. Discussion started: 10 April 2024

3.2 2.5xCH_{4SW} Fast Climate Response

Figure 3b-f shows global mean vertical response profiles from the fSST simulations for the four methane shortwave absorption perturbations (e.g., 2.5xCH_{4SW}). Relative to 2xCH_{4SW}, 2.5xCH_{4SW} yields slightly larger QRS increases (Fig. 3b) in the upper troposphere/lower stratosphere, as well as slightly larger QRS decreases in the lower-troposphere. This is consistent with the aforementioned instantaneous QRS profile response (Fig. 3a). These changes are associated with temperature (Fig. 3c) and relative humidity (RH; Fig. 3d) changes that favor increases in low-level cloud cover (CLOUD; Fig. 3e) that peak near 800 hPa and decreases in high-level cloud cover (e.g., for pressures < 300 hPa). Both of these CLOUD responses act to cool the surface. Compared to 2xCH_{4SW}, these cloud changes are generally larger under 2.5xCH_{4SW} (and become even larger under the larger methane perturbations). For example, 2.5xCH_{4SW} yields a decrease in global mean lower-tropospheric (pressures > 800 hPa) temperature of -0.02 K (not significant at the 90% confidence level) and an increase in upper-tropospheric (between 100 and 500 hPa) temperature of 0.08 K (significant at the 99% confidence level). Similarly, global mean lower-tropospheric RH increases by 0.01% and upper-tropospheric RH decreases by -0.08% (however, both changes are not significant at the 90% confidence level). Global mean lower-tropospheric CLOUD increases by 0.04% (significant at the 90% confidence level) and upper-tropospheric CLOUD decreases by -0.06% (significant at the 99% confidence level).

Correlations between the 2.5xCH_{4SW} global mean vertical response profiles show significant correlations. For example, the correlation between the global mean vertical temperature and QRS response profile from 990 hPa to 100 hPa is 0.93. The corresponding correlation between temperature and RH is -0.89, and the corresponding correlation between RH and CLOUD is 0.80. Thus, an increase in SW heating is associated with warming whereas a decrease in SW heating is associated with cooling. Warming is associated with a decrease in RH whereas cooling is associated with an increase in RH. Furthermore, an increase in RH is associated with an increase in CLOUD whereas a decrease in RH is associated with a decrease in CLOUD. These results help to support the importance of atmospheric SW absorption in driving the CLOUD response through altered temperature and RH. Spatial correlations at specific pressure levels also yield similarly significant but somewhat weaker correlations (Supplementary Figure 1). For example, spatially correlating the global mean annual mean change in CLOUD with the corresponding change in RH yields significant correlations in the lower-troposphere ranging from 0.40 to 0.65, as well as in the upper-troposphere ranging

https://doi.org/10.5194/egusphere-2024-872
Preprint. Discussion started: 10 April 2024

from 0.71 to 0.81. Similar conclusions are obtained with the larger methane perturbations.

These cloud changes are similar to those that occur in response to absorbing aerosols like black carbon (i.e., the aerosol-cloud semi-direct effect; Amiri-Farahani et al., 2019; Allen et al., 2019). Black carbon solar heating warms and dries (decreased relative humidity) the free troposphere, which promotes less cloud cover in the mid- to upper-troposphere (Stjern et al., 2017). Cooling of the lower troposphere and warming aloft also suggest enhanced lower-tropospheric stability. As lower-tropospheric stability is a measure of the inversion strength that caps the boundary layer, enhanced lower-tropospheric stability traps more moisture in the marine boundary layer, allowing for enhanced cloud cover (e.g., Wood and Bretherton, 2006). Under 2.5xCH_{4SW}, global mean lower-tropospheric stability significantly increases (at the 95% confidence level) by 0.03 K. Larger increases in lower-tropospheric stability occur under the larger methane perturbation, e.g., 0.07 K under 10xCH_{4SW}. This increase in lower-tropospheric stability is consistent with the increase in low cloud cover, most of which occurs over the oceans (Supplementary Figure 2a,d). Furthermore, enhanced stability also suggests reduced convective mass flux in the mid/upper-troposphere. Although we did not archive convective mass flux, Fig. 3f shows changes in convective cloud cover (CONCLOUD). All methane perturbations show decreased CONCLOUD in the mid/upper troposphere (pressures < 800 hPa). CONCLOUD also increases in the lower-troposphere (peaking near 900 hPa). Although these CONCLOUD changes are weaker than those associated with CLOUD, their profiles are very similar, implying that changes in convection also contribute to changes in CLOUD.

3.3 2.5xCH_{4SW} Total Climate Response

Figure 4a-e shows global mean vertical total climate response profiles from the coupled ocean-atmosphere simulations for the four methane shortwave absorption perturbations (e.g., 2.5xCH_{4SW}). The QRS, RH and CLOUD responses are similar to those from the fSST simulation (Fig. 3), which further highlights the importance of rapid adjustments to the total climate response. Furthermore, 2.5xCH_{4SW} yields larger QRS increases (Fig. 4a) in the upper troposphere/lower stratosphere relative to 2xCH_{4SW}, as well as larger lower-tropospheric QRS decreases. Increases in low- and mid-level clouds (Fig. 4c; peaking near 800 hPa) and decreases in high-level clouds (for pressures < 300 hPa) occurs, both of which act to cool the surface (Fig. 4f). Cooling of the troposphere (Fig. 4b) is much more pronounced under

https://doi.org/10.5194/egusphere-2024-872
Preprint. Discussion started: 10 April 2024

$2.5xCH_{4SW}$ as compared to $2xCH_{4SW}$, and in better agreement to the larger CH_4 perturbations.

Relative to the fast responses discussed above, the total responses are generally larger and more significant in the lower (and mid) troposphere but weaker in the upper troposphere. This is in general consistent with allowing the surface to respond to the CH_{4SW} perturbation in the fully coupled ocean-atmosphere experiments, and in particular, the negative surface CH_{4SW} "ERFs" discussed in Section 3.1 (i.e., decrease in surface solar radiation). For example, the $2.5xCH_{4SW}$ total response features a decrease in global mean lower-tropospheric temperature (Fig. 4b) of -0.10 K which is significant at the 95% confidence level and about 5x as large as the cooling under the fast response (Fig. 3c). A non-significant decrease in upper-tropospheric temperature of -0.02 K occurs under the total response, in contrast to the upper-tropospheric warming under the fast response (Fig. 3c). Similarly, global mean lower-tropospheric RH (Fig. 4d) increases by 0.06% (significant at the 90% confidence level) under the $2.5xCH_{4SW}$ total response, with a non-significant change in upper-tropospheric RH of 0.0002%. Global mean lower-tropospheric CLOUD (Fig. 4c) increases by 0.12% (significant at the 99% confidence level) and upper-tropospheric CLOUD decreases by -0.05% (significant at the 99% confidence level). The corresponding changes under the fast response (Fig. 3) are muted in the lower-troposphere (i.e., smaller increases in RH and CLOUD) but augmented in the upper-troposphere (i.e., larger decreases in RH and CLOUD). The total response of CONCLOUD (Fig. 4e) is generally similar to the fast response (Fig. 3f), although the $2.5xCH_{4SW}$ total response lacks an increase in the lower-troposphere.

Global maps of the TAS and PRECIP total climate responses (from coupled ocean-atmosphere simulations) under $2.5xCH_{4SW}$ are shown in Figure 4f,g. The global mean TAS response is -0.10 K (significant at the 95% confidence level); the global mean PRECIP response is -0.008 mm d^{-1} (-0.27%) which is not significant at the 90% confidence level. Comparing these $2.5xCH_{4SW}$ responses to the corresponding $2.5xCH_{4LW}$ responses of 0.35 K and 0.012 mm d^{-1} shows that under $2.5xCH_4$, methane shortwave absorption offsets 29% of the surface warming and 66% of the precipitation increase associated with its longwave radiative effects. We briefly note that some small areas of surface warming occur, e.g. central Canada/US. This warming is related to changes in atmospheric circulation, including an atmospheric ridge pattern in tropospheric geopotential heights (e.g., deepening of the Aleutian low to the west) and local decreases in low cloud cover and enhanced surface solar radiation over central Canada/US (not shown).

https://doi.org/10.5194/egusphere-2024-872
Preprint. Discussion started: 10 April 2024

We also note that the TAS response under $2.5xCH_{4SW}$, $5xCH_{4SW}$ and $10xCH_{4SW}$ approximately scales with every doubling of atmospheric methane concentrations. That is, going from $2.5xCH_{4SW}$ to $5xCH_{4SW}$ yields approximately double the surface cooling (-0.10 to -0.23 K); similarly going from $5xCH_{4SW}$ to $10xCH_{4SW}$ yields approximately another doubling of the surface cooling (-0.23 to -0.40 K). Similar conclusions apply for the TOA SW IRF, which approximately doubles from $2.5xCH_{4SW}$ to $5xCH_{4SW}$ (0.06 to 0.14 W m^{-2}), as well as from $5xCH_{4SW}$ to $10xCH_{4SW}$ (0.14 to 0.27 W m^{-2}). Similarly, the ERF associated with methane SW absorption (which as mentioned above includes CH_4 SW absorption and the impact of this SW absorption on CH_4 LW adjustments) increases from -0.10 W m^{-2} under $2.5xCH_{4SW}$ to -0.22 W m^{-2} under $5xCH_{4SW}$, and to -0.44 W m^{-2} under $10xCH_{4SW}$.

3.4 $2.5xCH_{4SW}$ Climate Feedbacks

We apply the radiative kernel decomposition to the $2.5xCH_{4SW}$ coupled ocean-atmosphere simulation (Figure 5). The 'fast' responses from the fixed climatological SST runs (i.e., the rapid adjustments) and the surface-temperature-induced 'slow' climate feedbacks (i.e., the difference between the coupled ocean atmosphere and fixed climatological SST simulations) are also included. Here, a positive feedback has the same meaning as a positive ADJ, as both represent a net energy increase. Similarly, a negative feedback has the same meaning as a negative ADJ, as both represent a net energy decrease. As with the larger methane perturbations, the cloud rapid adjustment and the cloud slow feedback under $2.5xCH_{4SW}$ are both negative at -0.12 W m^{-2} and -0.28 W m^{-2}, respectively. This implies that surface cooling in response to $2.5xCH_{4SW}$ radiative effects is largely due to the cloud rapid adjustment and cloud feedbacks.

As mentioned in Section 3.1, the $2.5xCH_{4SW}$ stratospheric temperature adjustment under fixed climatological SSTs also significantly contributes (at -0.04 W m^{-2}; about 1/3 the magnitude of the cloud adjustment) to the total rapid adjustment. This negative stratospheric temperature adjustment is consistent with the relatively large increase in stratospheric shortwave heating (Fig. 3b) and warming (Fig. 3c), which results in enhanced outgoing longwave radiation (i.e., loss of energy and a negative adjustment). The tropospheric temperature adjustment (Fig. 5) is also negative but not significant at the 90% confidence level at -0.03 W m^{-2}. In contrast, the surface temperature adjustment at +0.02 W m^{-2} (associated with cooling of the land surfaces and subsequent reduction in upwards longwave radiation) acts to weakly mute the negative total rapid adjustment. The other $2.5xCH_{4SW}$ rapid adjustment components are relatively small and not significant at the 90% confidence level.

https://doi.org/10.5194/egusphere-2024-872
Preprint. Discussion started: 10 April 2024

In terms of the 2.5xCH_{4SW} slow feedback, in addition to the dominant negative contribution from clouds, the water vapor and surface albedo feedback also significantly contribute to the negative total feedback at -0.09 and -0.03 W m^{-2}, respectively (Fig. 5). These are associated with tropospheric/surface cooling, resulting in less water vapor (a greenhouse gas) and enhanced snow/ice over land (enhanced albedo). In contrast, the tropospheric temperature and surface temperature adjustments are both significant and positive at 0.25 and 0.05 W m^{-2}, respectively, and act to mute the total negative feedback.

Decomposing the 2.5xCH_{4SW} cloud rapid adjustment into shortwave and longwave radiation components (not shown), we find the cloud rapid adjustment for shortwave radiation is -0.08 W m^{-2} and the cloud adjustment for longwave radiation is -0.05 W m^{-2} (both significant at the 90% confidence level). Thus, both shortwave and longwave cloud radiative components contribute similarly to the negative cloud rapid adjustment. Decomposing the slow cloud feedback into shortwave and longwave radiation components, we find corresponding values of -0.31 and 0.04 W m^{-2}, respectively. Here, the negative cloud feedback is largely due to cloud shortwave radiative effects, which is partially muted by cloud longwave radiative effects. These changes are qualitatively consistent with the 2.5xCH_{4SW} CLOUD changes discussed in Section 3.3, under the broad assumption that low clouds primarily reflect shortwave radiation and high clouds primarily inhibit outgoing longwave radiation. 2.5xCH_{4SW} CLOUD changes under the fast response (Fig. 3e) are augmented in the upper-troposphere (larger decreases in high-level cloud) as compared to the total response (Fig. 4c) and in particular the slow (Supplementary Figure 3c; Supplementary Figure 4d) response. The weaker decrease in upper-level clouds under the slow response is consistent with a lack of an increase in upper-tropospheric shortwave heating rate (Supplementary Fig. 4a). These statements are clearer under 10xCH_{4SW} (Supplementary Figure 3f; Supplementary Figure 5). In contrast, CLOUD changes under the total response (and slow feedback) are augmented in the low to mid-troposphere (larger increases in low to mid-level cloud) as compared to the fast response. The larger increase in low-level cloud under the slow response (most of which occurs over marine stratocumulus regions off the North and South American western coasts; Supplementary Figure 3a,d) is consistent with a low-level cloud positive feedback i.e., surface cooling promotes more low clouds and in turn, more cooling, etc. (Clement et al., 2009; Zelinka et al., 2020).

To summarize, we find that the shortwave absorption associated with the present-day methane perturbation (2.5xCH_4) offsets 19% of the ERF, 29% of the surface warming and 66% of the precipitation increase associated with its longwave

https://doi.org/10.5194/egusphere-2024-872
Preprint. Discussion started: 10 April 2024

radiative effects. These responses are associated with changes in the vertical profiles of shortwave heating (i.e., increases for pressures < 700 hPa and decreases for pressures > 700 hPa) which impacts atmospheric temperature, relative humidity and cloud cover. Our 2.5xCH_{4SW} results are therefore qualitatively consistent with those based on the larger 5xCH_4 and 10xCH_4 perturbations showed in A23.

3.5 Additional Analysis of the Precipitation Response

Precipitation responses can be understood from an energetic perspective (Muller and O'Gorman, 2011; Richardson et al., 2016; Liu et al., 2018). Precipitation is related to the diabatic cooling and the dry static energy flux divergence of the atmosphere as $L_cP = Q + H$, where L_c is the latent heat of condensation of water vapor; P is precipitation; Q is the column integrated diabatic cooling excluding latent heating; and H is the column integrated dry static energy flux divergence. Q is estimated as LWC + SWC + SH, where LWC is the net longwave radiative cooling and SWC is the net shortwave radiative cooling from the atmospheric column (i.e., difference between top-of-atmosphere and surface); and SH is the net downwards sensible heat flux at the surface. H is estimated as the residual between L_cP and Q.

Figure 6a,b shows the atmospheric energy budget decomposition for the total, fast and slow responses under 10xCH_{4SW} and 2.5xCH_{4SW}. Under both CH_{4SW} perturbations, the decrease in global mean precipitation (i.e., the energy of precipitation L_cP) is dominated by the slow response. For example, under 2.5xCH_{4SW} L_cP decreases by -0.09 W m^{-2} under the fast response. This increases (in magnitude) to -0.15 W m^{-2} under the slow response (i.e., total decrease is -0.24 W m^{-2}). Although these 2.5xCH_{4SW} changes are not significant at the 90% confidence level, all three L_cP decreases are significant under 10xCH_{4SW} at -0.29, -0.83 and -1.12 W m^{-2}, respectively. The precipitation decrease under the slow response is associated with a significant decrease in net longwave atmospheric radiative cooling of -0.17 W m^{-2} for 2.5xCH_{4SW} and -1.03 W m^{-2} for 10xCH_{4SW} (i.e., anomalous longwave radiative warming) which is consistent with cooling of the troposphere (e.g., Supplementary Fig. 4b and 5b). The decrease in net longwave atmospheric radiative cooling under the slow response is weakly muted by an increase in net shortwave radiative cooling at 0.02 W m^{-2} for 2.5xCH_{4SW} and 0.30 W m^{-2} for 10xCH_{4SW} (i.e., anomalous shortwave radiative cooling), consistent with tropospheric cooling and decreases in atmospheric water vapor (i.e., specific humidity decreases throughout the troposphere under the slow response; Supplementary Fig. 4f and 5f). This yields less solar absorption by water vapor, i.e., QRS decreases in the mid- and upper-troposphere under the slow response

https://doi.org/10.5194/egusphere-2024-872
Preprint. Discussion started: 10 April 2024

(Supplementary Fig. 4a and 5a).

The CH_{4SW} decrease in L_cP under the fast response is associated with opposite changes in SWC and LWC, including dominance of the SWC term as opposed to the LWC term. This includes a significant SWC decrease of -0.17 W m^{-2} for 2.5xCH_{4SW} and -0.85 W m^{-2} for 10xCH_{4SW} (i.e., less shortwave radiative cooling), which is consistent with the enhanced solar absorption by CH_{4SW} under the fast response (e.g., Supplementary Fig. 4a and 5a). This is partially offset by an increase in LWC, consistent with mid- to upper-tropospheric warming and enhanced outgoing longwave radiation.

The L_cP decrease under the total response is associated with similar magnitude decreases in both SWC and LWC. This is particularly true for 10xCH_{4SW}, where the SWC term decreases by -0.55 W m^{-2} and the LWC term decreases by -0.51 W m^{-2}. Under 2.5xCH_{4SW}, the corresponding changes are not significant at -0.15 and -0.08 W m^{-2}, respectively. In all cases, the H term is near zero in the global mean (i.e., energy transport in global mean should be zero). Similarly, the SH term is generally small in all cases.

To summarize these results, the decrease in global mean precipitation under CH_{4SW} is associated with both the fast and slow response, with most of the precipitation decrease related to the slow (surface temperature mediated) response. The decrease in precipitation under the fast response is largely due to the enhanced solar absorption by CH_{4SW} (decrease in the SWC term above), i.e., as atmospheric solar absorption increases, net atmospheric radiative cooling decreases, which leads to a decrease in precipitation. In contrast, the decrease in precipitation under the slow response is largely due to cooling of the troposphere and a decrease in net longwave atmospheric radiative cooling (decrease in the LWC term above).

The importance of both the fast and slow response (and the dominance of the slow response) in driving less global mean precipitation under CH_{4SW} is in contrast to other shortwave absorbers such as black carbon. With idealized black carbon perturbations, for example, the fast and slow global mean precipitation responses oppose one another. The fast response (associated with black carbon atmospheric solar absorption) yields a global mean decrease in precipitation whereas the weaker slow response (associated with surface warming) yields an increase in global mean precipitation (Samset et al., 2016; Stjern et al., 2017). The net result is a decrease in global mean precipitation, largely due to the fast response and enhanced atmospheric solar absorption by black carbon.

Thus, the main difference between the black carbon and CH_{4SW} impact on global

https://doi.org/10.5194/egusphere-2024-872
Preprint. Discussion started: 10 April 2024

mean precipitation is related to the slow response. Black carbon warms the surface which mutes the overall decrease in global mean precipitation (from the fast response). In contrast, CH_{4SW} cools the surface, which adds to the overall decrease in global mean precipitation (and contributes more to the decrease than does the fast response). We suggest this difference is related to differences in the vertical QRS profile. Under CH_{4SW}, QRS heating aloft encourages less precipitation whereas QRS cooling (e.g., Fig. 3a,b) below (pressures < 700 hPa) encourages tropospheric/surface cooling and a decrease in precipitation. Under black carbon, the QRS profile is more vertically uniform with increases throughout the atmosphere (e.g., Supplementary Figure 4 from Stjern et al., 2017). As with CH_{4SW}, black carbon QRS heating aloft encourages less precipitation whereas black carbon QRS heating below encourages surface warming and an increase in precipitation. Implicit in this argument is that the differences in the vertical solar heating profile between black carbon and CH_{4SW} also drive the different surface/tropospheric temperature responses (i.e., warming under black carbon but cooling under CH_{4SW}).

3.6 Comparisons with CO_{2SW}

In addition to CH_4, other greenhouse gases (GHGs), including carbon dioxide (CO_2), also absorb solar radiation. As with most climate models, CESM2 (via RRTMG) includes a representation of CO_2 SW absorption. In particular, RRTMG includes CO_2 SW absorption in four NIR/mid-IR bands: 1.3-1.6 μm, 1.9-2.15 μm, 2.5-3.1 μm and 3.8-12.2 μm. As mentioned above, RRTMG underestimates CO_2 SW IRF by 25-45% (Hogan and Matricardi, 2020).

Prior studies (focused on the radiative forcing) have shown the SW absorption effects of the present-day CO_2 perturbation are relatively small (Myhre et al., 1998; Etminan et al., 2016; Shine et al., 2022). For example, from the perspective of the SARF at the tropopause, CO_2 SW absorption yields a negative forcing that acts to decrease the magnitude of the CO_2 LW forcing by about 5% (Myhre et al., 1998; Etminan et al., 2016). This is largely due to direct SW absorption in the stratosphere dominating over relatively weak increases in tropospheric SW absorption due to overlap with water vapor (Etminan et al., 2016). The former acts to decrease downward SW at the tropopause (leading to a negative contribution that dominates the net effect), whereas the latter decreases upwards SW at the tropopause (leading to a smaller, positive forcing). The direct SW absorption in the stratosphere, by reducing LW cooling, also affects the temperature adjustment (i.e., the LW flux from the stratosphere to the troposphere is increased). As shown by Etminan et al. (2016), the overall negative contribution due to CO_{2sw} is due to

https://doi.org/10.5194/egusphere-2024-872
Preprint. Discussion started: 10 April 2024

the dominance of its 2.7 µm band. In contrast, for CH_{4sw}, the overall positive SW forcing is due to both its 1.7 and 2.3 µm bands. This contrasting behavior between CO_{2SW} and CH_{4SW} is largely driven by the amount of overlap of the SW absorption bands with the near-IR absorption bands for water vapor (Etminan et al., 2016).

To gain a better understanding of the importance of the SW absorption effects due to CH_4 relative to CO_2, we repeat our suite of CESM2 experiments, but based on idealized CO_2 perturbations, including 2x and 4x preindustrial atmospheric CO_2 concentrations. This includes two sets of identical experiments (e.g., Table 1), one that includes CO_2 LW+SW radiative effects (e.g., $2xCO_2^{EXP}$) and one that lacks CO_2 SW radiative effects (e.g., $2xCO_{2NOSW}^{EXP}$). CO_2 SW absorption in the four NIR/mid-IR bands in RRTMG is turned off in the simulations that lack CO_2 SW radiative effects. These are compared to the default preindustrial control experiment (PIC^{EXP}), which includes CO_2 (and CH_4) LW+SW radiative effects, as well as to a new preindustrial control experiment with CO_2 SW radiative effects turned off (i.e., LW effects only, denoted as $PIC_{NOCO2SW}^{EXP}$). As with the methane perturbations, this suite of CO_2 simulations allows quantification of the CO_2 LW+SW, LW and SW radiative effects, denoted for example as $2xCO_{2LW+SW}$, $2xCO_{2LW}$ and $2xCO_{2SW}$. The $2xCO_{2LW+SW}$ signal is obtained by subtracting the default $2xCO_2$ perturbation from the default control ($2xCO_2^{EXP} - PIC^{EXP}$). The $2xCO_{2LW}$ signal is obtained by subtracting the $2xCO_2$ perturbation without CO_2 SW absorption from the corresponding control simulation without CO_2 SW absorption ($2xCO_{2NOSW}^{EXP} - PIC_{NOCO2SW}^{EXP}$). The $2xCO_{2SW}$ signal is obtained by taking the double difference, i.e., $(2xCO_2^{EXP} - PIC^{EXP}) - (2xCO_{2NOSW}^{EXP} - PIC_{NOCO2SW}^{EXP})$.

We note here that it is difficult to directly compare our CH_4 and CO_2 results. For example, $2.5xCH_4$ represents an increase of ~0.0012 ppm whereas $2xCO_2$ represents an increase of ~560 ppm. Nonetheless, we provide a qualitative comparison below, with emphasis on the proportion of LW radiative effects offset by SW radiative effects for each GHG.

Figure 7 shows the corresponding TOA radiative fluxes and rapid adjustments for both $2xCO_2$ and $4xCO_2$. As expected, these perturbations yield a large positive TOA LW IRF at 2.59 W m^{-2} for $2xCO_2$ and 5.30 W m^{-2} for $4xCO_2$. The corresponding TOA SW IRFs are also positive, but they are much smaller at 0.03 and 0.05 W m^{-2}, respectively (only the latter is significant at the 90% confidence level). The total rapid adjustment for both CO_2 perturbations is negative under SW radiative effects at -0.06 W m^{-2} for $2xCO_2$ and -0.40 W m^{-2} for $4xCO_2$. The larger

https://doi.org/10.5194/egusphere-2024-872
Preprint. Discussion started: 10 April 2024

negative total ADJ offsets the less positive IRF, leading to a negative ERF at -0.03 W m^{-2} for $2xCO_{2SW}$ and -0.35 W m^{-2} for $4xCO_{2SW}$ (only the latter is significant at the 90% confidence level).

These results are qualitatively consistent with $2.5xCH_{4SW}$ (Fig. 2), including a negative ADJ that offsets the positive IRF, leading to a negative ERF. The methane SW radiative effect, however, represents a larger percentage of its LW radiative effect. As discussed above, $2.5xCH_{4SW}$ (and the larger methane perturbations from A23) offsets ~20% of the positive ERF associated with $2.5xCH_{4LW}$. This is due to a relatively strong negative rapid adjustment associated with CH_{4SW} (e.g., -0.16 W m^{-2} for $2.5xCH_{4SW}$, which increases to -0.77 W m^{-2} for $10xCH_{4SW}$). This, in turn, drives the negative CH_{4SW} ERF.

In contrast, $2xCO_{2SW}$ and $4xCO_{2SW}$ offset only 0.7% and 4%, respectively, of the positive ERF associated with their LW radiative effects. The weaker CO_{2SW} muting of CO_{2LW} ERF is related to a relatively weak CO_{2SW} negative adjustment (-0.06 W m^{-2} for $2xCO_{2SW}$, but increasing to -0.40 W m^{-2} for $4xCO_{2SW}$), that leads to a relatively weak negative CO_{2SW} ERF. The weaker CO_{2SW} muting of CO_{2LW} ERF is also related to the relatively large and positive CO_{2LW} ERF. This large and positive CO_{2LW} ERF is due to a relatively large and positive ADJ under CO_{2LW} (largely due to the stratospheric temperature adjustment, as well as clouds; Fig. 7) which reinforces the relatively large and positive CO_{2LW} IRF. For example, $2xCO_{2LW}$ yields an ADJ of 1.55 W m^{-2} and a corresponding ERF of 4.15 W m^{-2}. Thus, the weaker CO_{2SW} muting of CO_{2LW} ERF is related to a relatively weak SW radiative effect, particularly compared to its very strong LW radiative effect.

We also note that the negative total rapid adjustment due to CO_2 SW absorption is dominated by a negative stratospheric temperature adjustment (Fig. 7c,d). This is also in contrast to methane, where clouds (followed by the stratospheric temperature adjustment) drive most of the negative total rapid adjustment under SW radiative effects (Fig. 2b). For $4xCO_{2SW}$, the stratospheric adjustment is -0.46 W m^{-2} as compared to -0.19 W m^{-2} for clouds. This larger negative stratospheric adjustment under $4xCO_{2SW}$ is consistent with relatively large shortwave heating above ~200 hPa (to be discussed below).

The ERF, IRF and ADJ under $2xCO_2$ LW+SW radiative effects shown here compare well with those from PDRMIP (Smith et al., 2018), although CESM2 yields a larger positive ADJ (and ERF). For example, PDRMIP yields a multi-model mean IRF, ERF and ADJ of ~2.5, 3.7 and 1.2 W m^{-2}, respectively. The corresponding values from our $2xCO_2$ CESM2 simulation are 2.6, 4.1 and 1.6 W m^{-2}. The bulk of CESM2's larger ADJ is due to a larger cloud adjustment at 0.98

W m^{-2} compared to 0.45 W m^{-2} for PDRMIP.

Figure 8a shows the global mean instantaneous shortwave heating rate profile for $2xCO_{2SW}$ and $4xCO_{2SW}$. Both profiles show a decrease in QRS throughout the troposphere with two minima, one near 800 hPa in the lower-troposphere and another near 250 hPa in the upper troposphere. Above 200 hPa, QRS increases rapidly through the stratosphere, reaching ~0.15 K d^{-1} at 3.6 hPa under $4xCO_{2SW}$. The vertical structure of QRS under CO_{2SW} shows similarities to that under CH_{4SW} (Fig. 3a), but CO_{2SW} exhibits QRS decreases throughout the entire troposphere as well as relatively large QRS increases in the stratosphere. In other words, the transition level from decreasing to increasing QRS occurs higher aloft under CO_{2SW}, with larger QRS increases in the stratosphere.

The corresponding fSST 'fast' responses are included in Figure 8b-f. The QRS profile (Fig. 8b) is very similar to the corresponding instantaneous profile (Fig. 8a). The relatively large CO_{2SW} stratospheric solar heating helps to explain the correspondingly large negative stratospheric temperature adjustment (Fig. 7c,d). That is, the large increase in stratospheric solar absorption leads to corresponding warming and subsequently, enhanced outgoing longwave radiation which acts to cool the climate system. The decrease in tropospheric QRS is associated with weak cooling (Fig. 8c), and increases in both relative humidity (Fig. 8d) and clouds (Fig. 8e), with stronger responses under $4xCO_{2SW}$ as compared to $2xCO_{2SW}$. The opposite responses occur in the stratosphere. These results again share similarities to those based on CH_{4SW} (Fig. 3), but CO_{2SW} exhibits more uniform changes throughout the troposphere (i.e., the transition level occurs higher aloft), as well as relatively large stratospheric changes.

Due to the relatively weak and non-significant $2xCO_{2SW}$ radiative fluxes (and limited computational resources), we only perform the coupled ocean-atmosphere simulations for $4xCO_2$. Figure 9a-c shows the global mean total, fast and slow response vertical profiles under $4xCO_{2SW}$ for QRS, temperature and cloud cover. Significant cooling (Fig. 9b) occurs under the total (and slow) response throughout the troposphere, with maximum cooling of ~0.5 K near 200 hPa under the total response. Above this level, cooling gradually weakens and transitions into warming aloft, peaking at ~1 K near 50 hPa. This vertical temperature profile is consistent with the instantaneous (Fig. 8a) and fast QRS profile (Fig. 9a), but less with the QRS profile for the total climate response (Fig. 9a). The corresponding vertical CLOUD total response profile (Figure 9c) shows increasing cloud cover throughout the troposphere, with decreases aloft (near 100 hPa), generally similar to the fast response but with larger tropospheric CLOUD increases and weaker CLOUD decreases aloft.

The global maps of the TAS and PRECIP total climate response under $4xCO_{2SW}$ are included in Figure 9d,e. $4xCO_{2SW}$ drives a significant decrease in TAS and PRECIP at -0.38 K and -0.031 mm d^{-1} (-1.05%). However, when these responses are scaled by the $4xCO_{2SW}$ ERF (-0.35 W m^{-2}), the temperature and precipitation response per ERF are 1.09 K per W m^{-2} and 0.089 mm d^{-1} per W m^{-2}, which are nearly the same as those under $2.5xCH_{4SW}$ at 1.0 K per W m^{-2} and 0.080 mm d^{-1} per W m^{-2}. Similar values are also obtained for the two larger CH_4 perturbations at 1.05 and 0.90 K per W m^{-2} for 5x and $10xCH_{4SW}$, respectively (0.095 and 0.089 mm d^{-1} per W m^{-2} for PRECIP). The similar climate response per unit ERF is not unexpected, and is consistent with the general similarities (outside of the different transition levels and stratospheric differences) between the CO_{2SW} and CH_{4SW} instantaneous QRS profile, as well as similar climate feedbacks. For example, as with CH_{4SW}, the slow cloud response (i.e., the total response minus the fast response) under $4xCO_{2SW}$ is also negative at –0.31 W m^{-2} (Figure 10), acting to amplify the negative cloud rapid adjustment in both cases.

Although $4xCO_{2SW}$ and $2.5xCH_{4SW}$ yield very similar climate responses when normalized by the corresponding ERF, the $4xCO_{2SW}$ TAS and PRECIP responses are quite small as compared to the corresponding LW radiative effects at 5.84 K and 0.27 mm d^{-1} (9.1%), respectively. For example, if CH_{4LW} yielded the same 5.84 K of warming, this would correspond to surface cooling associated with CH_{4SW} of ~1.75K (assuming 30% offset, which may not apply here). The weaker effects of CO_{2SW} are illustrated in Figure 9f, which shows the $4xCO_{2SW}$ muting of $4xCO_{2LW}$ (as a percentage; to be compared to Figure 1e for $2.5xCH_4$). In terms of TAS, $4xCO_{2SW}$ mutes 6.5% of the warming due to LW radiative effects. For PRECIP, $4xCO_{2SW}$ mutes 11.5% of the increase in precipitation due to LW radiative effects. Thus, the muting effects of CO_{2SW} are much weaker than those associated with CH_{4SW}, where ~30% of the warming and ~60% of the wetting due to CH_4 LW radiative effects are offset.

We also perform the atmospheric energy balance calculation (Section 3.5) on the suite of $4xCO_{2SW}$ simulations (Fig. 6c). Overall, the conclusions discussed in Section 3.5 under $2.5xCH_{4SW}$ and $10xCH_{4SW}$ also apply under $4xCO_{2SW}$. The decrease in the global mean energy of precipitation under $4xCO_{2SW}$ (-0.92 W m^{-2} under the total response) is associated with both the fast (a non-significant decrease of -0.08 W m^{-2}) and slow response (-0.84 W m^{-2}). Here, nearly all of the precipitation decrease (91% as opposed to 63% for $2.5xCH_{4SW}$ and 74% for $10xCH_{4SW}$) is related to the slow (surface temperature mediated) response. In other words, only 9% of the precipitation decrease under $4xCO_{2SW}$ is due to the fast response, which is much lower than that under CH_{4SW} (26-37%). The weaker

https://doi.org/10.5194/egusphere-2024-872
Preprint. Discussion started: 10 April 2024

contribution to the decrease in total precipitation by the $4xCO_{2SW}$ fast response is consistent with similar (but opposite signed) changes in the SWC and LWC terms at -0.41 W m^{-2} and 0.35 W m^{-2}, respectively, which neutralize one another. This cancellation is consistent with the $4xCO_{2SW}$ solar heating profile (e.g., Fig. 8b) where nearly all of the heating occurs in the stratosphere. Thus, the added solar heating—although decreasing the SWC term—primarily warms the stratosphere where the energy is efficiently radiated back to space (i.e., the SWC decrease is primarily balanced by an increase in the LWC term). This is in contrast to the QRS profiles under CH_{4SW} (e.g., Fig. 3b) which show significant solar absorption throughout the mid- and upper troposphere (pressures < 700 hPa). Thus, we suggest the relatively weak decrease in precipitation under the $4xCO_{2SW}$ fast response (relative to the CH_{4SW} perturbations) is related to differences in the vertical QRS profile, with CO_{2SW} solar absorption primarily occurring in the stratosphere.

4 Discussion and Conclusions

We have expanded upon the work of A23, by explicitly simulating the radiative and climate responses of the present-day (2.5x preindustrial) perturbation of methane, decomposed into LW+SW, LW and SW radiative effects. Our results here based on $2.5xCH_4$ are consistent with the conclusions from A23, and re-emphasize the importance of methane SW absorption—not only under relatively large perturbations, but also under realistic, present-day perturbations.

Our new results suggest that the inferred muting of warming and wetting due to present-day methane shortwave absorption was underestimated in A23. Figure 1c,d compares the simulated versus regression-estimated present-day CH_4 temperature and precipitation responses. Surface cooling in response to the simulated $2.5xCH_{4SW}$ is -0.10 K, relative to the inferred estimate of -0.04 K. Although the simulated $2.5xCH_{4LW}$ warming at 0.35 K is also larger than that inferred at 0.22 K, the increase in simulated versus inferred cooling due to shortwave absorption represents a bigger fractional change. That is, the simulated $2.5xCH_{4SW}$ acts to mute 29% of the warming due to the corresponding methane longwave radiative effects; the corresponding muting under the inferred $2.5xCH_{4SW}$ is only 18% (Fig. 1e). Similar conclusions apply for precipitation, where 66% as opposed to 50% of the precipitation increase associated with methane longwave radiative effects under the present-day methane perturbation is offset by shortwave absorption (Fig. 1e). However, we reiterate that the global mean precipitation response under $2.5xCH_{4SW}$ at -0.008 mm d^{-1} (-0.27%) is not significant at the 90% confidence level. Nonetheless, similar to the larger methane

https://doi.org/10.5194/egusphere-2024-872
Preprint. Discussion started: 10 April 2024

perturbations emphasized in A23, SW absorption due to the present-day CH_4 perturbation offsets ~30% of the warming and ~60% of the precipitation increase associated with the present-day CH_4 LW radiative effects. Muting of warming and wetting is consistent with a negative CH_{4SW} ERF due to a negative rapid adjustment dominated by clouds. This in turn weakens the positive ERF associated with CH_{4LW}. Under the present-day methane perturbation, ~20% of the ERF associated with methane longwave radiative effects is muted by shortwave absorption, which is again similar to the larger CH_4 perturbations in A23.

An atmospheric energy budget analysis (Fig. 6) shows that the decrease in global mean precipitation under CH_{4SW} is associated with both the fast and slow response, with most of the precipitation decrease related to the slow (surface temperature mediated) response. The decrease in precipitation under the fast response is largely due to the enhanced solar absorption by CH_{4SW}, whereas the decrease in precipitation under the slow response is largely due to cooling of the surface/troposphere and a decrease in net longwave atmospheric radiative cooling. The importance of both the fast and slow response (and the dominance of the slow response) in driving less global mean precipitation under CH_{4SW} is in contrast to other shortwave absorbers such as black carbon, which we suggest is related to differences in the vertical QRS profile. That is, the CH_{4SW} QRS profile is positive for pressures < 700 hPa and negative for pressures > 700 hPa, whereas the black carbon QRS profile is more vertically uniform with increases throughout the atmosphere. The former promotes surface cooling and less precipitation whereas the latter promotes surface warming and more precipitation.

As many climate models lack methane SW absorption, our results imply that such models may overestimate the warming and wetting due to the increase in atmospheric methane concentrations over the historical time period. Similarly, such models may also have deficient simulation of the corresponding methane climate impacts under future climate projections.

We further show the importance of CH_{4SW} by comparison to CO_{2SW}. CO_2 SW absorption yields qualitatively similar results to CH_4 SW absorption, including a negative ADJ that offsets the positive IRF, leading to a negative ERF (Fig. 7). In contrast to CH_{4SW} (where the cloud adjustment dominates), the negative ADJ under CO_{2SW} is largely due to the stratospheric temperature adjustment, which is consistent with larger SW absorption in the stratosphere under CO_{2SW} (Fig. 8a). More importantly, the muting effect of methane SW absorption is much larger than that associated with CO_2 (e.g., Figure 9f). For example, $2xCO_{2SW}$ offsets only 0.7% of the ERF associated with $2xCO_{2LW}$. Under $4xCO_{2SW}$, the corresponding

https://doi.org/10.5194/egusphere-2024-872
Preprint. Discussion started: 10 April 2024

offset is 4%. Consistent with these results, $4xCO_{2SW}$ muting of the climate responses due to $4xCO_{2LW}$ are also relatively small (about five times smaller as compared to the $2.5xCH_{4SW}$ muting effects), at 6.5% for TAS and 11.5% for PRECIP. Although we have not performed a suite of present-day CO_2 simulations (i.e., ~$1.5xCO_2$) to compare to the present-day CH_4 simulations, the above results strongly suggest that the present-day CO_2 SW absorption effects are negligible (e.g., <1% muting of CO_{2LW} ERF under $2xCO_2$). In contrast, SW absorption associated with the present-day CH_4 perturbation is not negligible, and acts to offset a significant proportion of CH_4 LW radiative effects.

As our conclusions continue to be derived from one climate model, we encourage additional multi-model studies to evaluate the robustness of these results. Ideally, this includes simulations that include interactive chemistry (e.g., methane can enhance tropospheric ozone production), as our CESM2/CAM6 simulations do not. We also reiterate that there are known deficiencies in the shortwave radiative transfer code used in most climate model calculations, including CESM2. As mentioned above, CESM2's radiative transfer model (RRTMG) underestimates CH_4 (and CO_2) SW IRF by 25-45% (Hogan and Matricardi, 2020). This is in addition to the various subtleties in the quantification of methane shortwave forcing identified by Byrom and Shine (2022). These subtleties include the need for careful representation of the spectral variation of surface albedo and the vertical profile of methane, and the role of shortwave absorption at longer wavelengths, specifically methane's 7.6 μm band that is not included in some climate model radiation codes, including RRMTG. Thus, additional efforts are needed to improve climate model representation of CH_{4SW}.

In the context of the most recent IPCC ERF estimates, methane SW absorption is included and is based on Smith et al. (2018). The corresponding 1750-2019 (729.2 to 1866.3 ppb, or 2.6x increase) methane ERF is 0.54 ± 0.11 W m^{-2}, which includes a correction associated with methane SW absorption of -0.08 W m^{-2} (Forster et al., 2021). Our estimate for $2.5xCH_4$ is within this uncertainty range at 0.43 W m^{-2} (0.44 W m^{-2} if we include the surface temperature adjustment). Furthermore, we estimate the CH_{4SW} correction (i.e., the CH_{4SW} ERF) at -0.10 W m^{-2}, which compares very well to the IPCC estimate of -0.08 W m^{-2}. The most recent IPCC global warming potentials (GWP) for methane (e.g., 82.5 ± 25.8 for fossil-CH_4 and a 20-year time horizon) also include methane SW absorption. Given the caveats discussed above (e.g., underestimation of CH_4 SW IRF by 25-45%), however, these estimates of the CH_{4SW} adjustment and the corresponding climate effects may be underestimated.

https://doi.org/10.5194/egusphere-2024-872
Preprint. Discussion started: 10 April 2024

We also iterate that these are concentration ("abundance") based ERF estimates. The methane concentration used to derive such a concentration-based ERF is based on the observed change, which is influenced not only by the change in methane emissions, but also changes in emissions of other compounds that affect methane lifetime and concentrations (Stevenson et al., 2020). For example, changes in non-methane ozone precursors including nitrogen oxides and volatile organic compounds in general reduce methane concentrations. This means that the methane perturbation applied here is smaller than that which would arise if methane is emissions-driven. In the latter case, the derived methane concentration change would be higher than that observed, would take account of the impact of methane on its own lifetime, and would be attributable to the change in methane emissions alone. For example, Shindell et al. (2005) shows that the instantaneous tropopause direct radiative forcing (1998 relative to preindustrial) of methane alone increases from 0.48 to 0.59 W m^{-2}, in switching from a concentration-based to an emissions-based perspective. Accounting for the impacts of methane on ozone production and stratospheric water vapor further increases methane's radiative forcing to ~0.9 W m^{-2} (Shindell et al., 2005). A more recent estimate of the emissions-based methane ERF (including indirect effects) is 1.19±0.38 W m^{-2} (Szopa et al., 2021). This is due to indirect positive ERFs from methane enhancing its own lifetime, enhancing stratospheric water vapor, causing ozone production, and influencing aerosols and the lifetimes of hydrochlorofluorocarbons (HCFCs) and hydrofluorocarbons (HFCs) (Myhre et al., 2013; O'Connor et al., 2022). We reiterate that our simulations do not include these methane indirect effects.

Despite our main conclusion—that the present-day methane perturbation is associated with CH_{4SW} muting of ~30% of the CH_{4LW} surface warming—we emphasize that methane remains a potent GHG. Continued efforts to reduce CH_4 emissions are vital for staying below 1.5°C of global warming.

Code Availability

CESM2 can be downloaded from NCAR at https://www.cesm.ucar.edu/models/cesm2/download. The Python-based radiative kernel toolkit and the GFDL radiative kernel can be downloaded from https://climate.rsmas.miami.edu/data/radiative-kernels/.

Data Availability

A core set of model data from the 2.5x preindustrial methane CESM2 simulations is available here: https://doi.org/10.5281/zenodo.10357888.

Author Contributions

R.J.A performed CESM2/CAM6 simulations and analyzed the results. All authors, including X.Z., C.A.R., C.J.S., R.J.K and B.H.S discussed the results and contributed to the writing.

Competing Interests

The authors declare no competing interests.

Acknowledgements

R. J. Allen is supported by NSF grant AGS-2153486. We would like to acknowledge high-performance computing support from Cheyenne (doi:10.5065/D6RX99HX) provided by NCAR's Computational and Information Systems Laboratory, sponsored by the National Science Foundation. We also acknowledge helpful comments and discussions with Keith Shine, Universtiy of Reading.

References

Allen, R. J., Zhao, X., Randles, C. A., Kramer, R. J., Samset, B. H. & Smith, C. J.: Surface warming and wetting due to methane's long-wave radiative effects muted by short-wave absorption. *Nat. Geosci.*, **16**, 314-320, doi: 10.1038/s41561-023-01144-z, 2023.

Allen, R. J., Amiri-Farahani, A., Lamarque, J-F., Smith, C., Shindell, D., Hassan, T. & Chung, C. E.: Observationally-constrained aerosol–cloud semi-direct effects. *npj Clim. Atmos. Sci.*, **2**, 16, doi: 10.1038/s41612-019-0073-9, 2019.

Amiri-Farahani, A., Allen, R. J., Li, K.-F. & Chu, J.-E.: The semidirect effect of combined dust and sea salt aerosols in a multimodel analysis. *Geophys. Res. Lett.* **46**, 10512–10521, 2019.

Byrom, R. E. & Shine, K. P.: Methane's solar radiative forcing. *Geophys. Res.*

https://doi.org/10.5194/egusphere-2024-872
Preprint. Discussion started: 10 April 2024

Lett., **49**, e2022GL098270, doi: 10.1029/2022GL098270, 2022.

Clement, A., Burgman, R. & Norris, J. R.: Observational and model evidence for positive low-level cloud feedback. *Science*, **325**, 460-464, 2009.

Collins, W. D., Feldman, D. R., Kuo, C. & Nguyen, N. H.: Large regional shortwave forcing by anthropogenic methane informed by Jovian observations. *Sci. Adv.* **4**, eaas9593, 2018.

Conley, A. J., Lamarque, J.-F., Vitt, F., Collins, W. D. & Kiehl, J.: PORT, a CESM tool for the diagnosis of radiative forcing. *Geosci. Model Dev.* **6**, 469–476, 2013.

Danabasoglu, G., Lamarque, J.-F., Bacmeister, D., Bailey, D. A., & et al.: The Community Earth System Model version 2 (CESM2). *J. Adv. Model. Earth Syst.* **12**, e2019MS001916, 2020.

Etminan, M., Myhre, G., Highwood, E. J. & Shine, K. P.: Radiative forcing of carbon dioxide, methane, and nitrous oxide: a significant revision of the methane radiative forcing. *Geophys. Res. Lett.* **43**, 12614–12623, 2016.

Forster, P., T. Storelvmo, K. Armour, W. Collins, J.-L. Dufresne, D. Frame, D.J. Lunt, T. Mauritsen, M.D. Palmer, M. Watanabe, M. Wild, and H. Zhang, 2021: The Earth’s Energy Budget, Climate Feedbacks, and Climate Sensitivity. In *Climate Change 2021: The Physical Science Basis. Contribution of Working Group I to the Sixth Assessment Report of the Intergovernmental Panel on Climate Change* [Masson-Delmotte, V., P. Zhai, A. Pirani, S.L. Connors, C. Péan, S. Berger, N. Caud, Y. Chen, L. Goldfarb, M.I. Gomis, M. Huang, K. Leitzell, E. Lonnoy, J.B.R. Matthews, T.K. Maycock, T. Waterfield, O. Yelekçi, R. Yu, and B. Zhou (eds.)]. Cambridge University Press, Cambridge, United Kingdom and New York, NY, USA, pp. 923–1054, doi:10.1017/9781009157896.009.

Forster, P. M., Richardson, T., Maycock, A. C., Smith, C. J., Samset, B. H., Myhre, G., Andrews, T., Pincus, R. & Schulz, M.: Recommendations for diagnosing effective radiative forcing from climate models for CMIP6. *J. Geophys. Res. Atmos.* **121**, 12460–12475, 2016.

Hogan, R. J. & Matricardi, M.: Evaluating and improving the treatment of gases in radiation schemes: the Correlated K-Distribution Model Intercomparison Project (CKDMIP). *Geosci. Model Dev.* **13**, 6501–6521, 2020.

Iacono, M. J., Delamere, J. S., Mlawer, E. J., Shephard, M. W., Clough, S. A. & Collins, W. D.: Radiative forcing by long-lived greenhouse gases: calculations

https://doi.org/10.5194/egusphere-2024-872
Preprint. Discussion started: 10 April 2024

with the AER radiative transfer models. *J. Geophys. Res. Atmos.* **113**, D13103, 2008.

Kramer, R. J., Matus, A. V., Soden, B. J. & L'Ecuyer, T. S.: Observation-based radiative kernels from CloudSat/CALIPSO. *J. Geophys. Res. Atmos.* **124**, 5431–5444, 2019.

Li, J., Curry, C. L., Sun, Z. & Zhang, F.: Overlap of solar and infared spectra and the shortwave radiative effect of methane. *J. Atmos. Sci.* **67**, 2372-2389, 2010.

Liu, L., Shawki, D., Voulgarakis, A., Kasoar, M., Samset, B. H., Myhre, G., & et al.: A PDRMIP multimodel study on the impacts of regional aerosol forcings on global and regional precipitation. *J. Climate*, ***31***, 4429-4447, 2018.

Muller, C., & O'Gorman, P.: An energetic perspective on the regional response of precipitation to climate change. *Nature Climate Change* 1, 266–271, doi: 10.1038/nclimate1169, 2011.

Myhre, G. et al., 2013: Anthropogenic and Natural Radiative Forcing. In: *Climate Change 2013: The Physical Science Basis. Contribution of Working Group I to the Fifth Assessment Report of the Intergovernmental Panel on Climate Change* [Stocker, T.F., D. Qin, G.-K. Plattner, M. Tignor, S.K. Allen, J. Boschung, A. Nauels, Y. Xia, V. Bex, and P.M. Midgley (eds.)]. Cambridge University Press, Cambridge, United Kingdom and New York, NY, USA, pp. 659–740, doi:10.1017/cbo9781107415324.018.

Myhre, G., Forster, P. M., Samset, B. H., & et al., 2017: PDRMIP: a Precipitation Driver and Response Model Intercomparison Project—protocol and preliminary results. *Bull. Am. Meteorol. Soc.* **98**, 1185–1198, 2017.

Myhre, G., E. Highwood, Shine, K. & Stordal, F.: New estimates of radiative forcing due to well mixed greenhouse gases, *Geophys. Res. Lett.*, **25**(14), 2715-2718, doi:10.1029/98GL01908, 1998.

O'Connor, F. M., Johnson, B. T., Jamil, O., Andrews, T., Mulcahy, J. P., & Manners, J.: Apportionment of the pre-industrial to present-day climate forcing by methane using UKESM1: The role of the cloud radiative effect. *Journal of Advances in Modeling Earth Systems*, **14**, e2022MS002991, doi:10.1029/2022MS002991, 2022.

https://doi.org/10.5194/egusphere-2024-872
Preprint. Discussion started: 10 April 2024

Richardson, T. B., Forster, P. M., Andrews, T. & Parker, D. J.: Understanding the rapid precipitation response to CO2 and aerosol forcing on a regional scale. *J. Climate*, **29,** 583–594, doi: 10.1175/JCLI-D-15-0174.1, 2016.

Samset, B. H., Myhre, G., Forster, P. M., Hodnebrog, Ø., Andrews, T., Faluvegi, G, & et al.: Fast and slow precipitation responses to individual climate forcers: A PDRMIP multimodel study. *Geophys. Res. Lett.*, **43**, 2782-2791, doi:10.1002/2016GL068064, 2016.

Shindell, D. T., Faluvegi, G., Bell, N. & Schmidt, G. A.: An emissions-based view of climate forcing by methane and tropospheric ozone. *Geophys. Res. Lett.*, **32**, L04803, doi: 10.1029/2004GL021900, 2005.

Shine, K. P., Byrom, R. E., & Checa-Garcia, R.: Separating the shortwave and longwave components of greenhouse gas radiative forcing. *Atmospheric Science Letters*, 23(10), e1116, doi: 10.1002/asl.1116, 2022.

Smith, C. J., Kramer, R. J., Myhre, G. & et al.: Understanding rapid adjustments to diverse forcing agents. *Geophys. Res. Lett.* **45**, 12023–12031, 2018.

Smith, C. J., Kramer, R. J., Myhre, G. & et al.: Effective radiative forcing and adjustments in CMIP6 models. *Atmos. Chem. Phys.* **20**, 9591–9618, 2020.

Soden, B. J., Held, I. M., Colman, R. & et al.: Quantifying climate feedbacks using radiative kernels. *J. Clim.* **21**, 3504–3520, 2008.

Stevenson, D. S., Zhao, A., Naik, V., O'Connor, F. M., Tilmes, S., Zeng, G., Murray, L. T., Collins, W. J., Griffiths, P. T., Shim, S., Horowitz, L. W., Sentman, L. T., & Emmons, L.: Trends in global tropospheric hydroxyl radical and methane lifetime since 1850 from AerChemMIP. *Atmos. Chem. Phys*., **20**, 12905–12920, doi:10.5194/acp-20-12905-2020, 2020.

Stjern, C. W., Samset, B. H., Myhre, G., Forster, P. M. & et al.: Rapid adjustments cause weak surface temperature response to increased black carbon concentrations. *Journal of Geophysical Research: Atmospheres*. **122**, 11,462–11,481, doi:10.1002/2017JD027326, 2017.

Szopa, S., V. Naik, B. Adhikary, P. Artaxo, T. Berntsen, W.D. Collins, S. Fuzzi, L. Gallardo, A. Kiendler-Scharr, Z. Klimont, H. Liao, N. Unger, and P. Zanis, 2021: Short-Lived Climate Forcers. In *Climate Change 2021: The Physical Science*

https://doi.org/10.5194/egusphere-2024-872
Preprint. Discussion started: 10 April 2024

Basis. Contribution of Working Group I to the Sixth Assessment Report of the Intergovernmental Panel on Climate Change [Masson-Delmotte, V., P. Zhai, A. Pirani, S.L. Connors, C. Péan, S. Berger, N. Caud, Y. Chen, L. Goldfarb, M.I. Gomis, M. Huang, K. Leitzell, E. Lonnoy, J.B.R. Matthews, T.K. Maycock, T. Waterfield, O. Yelekçi, R. Yu, and B. Zhou (eds.)]. Cambridge University Press, Cambridge, United Kingdom and New York, NY, USA, pp. 817–922, doi:10.1017/9781009157896.008.

Wood, R. & Bretherton, C. S.: On the Relationship between Stratiform Low Cloud Cover and Lower-Tropospheric Stability. *J. Climate*, **19**, 6425–6432, doi:10.1175/JCLI3988.1, 2006.

Zelinka, M. D., Myers, T. A., McCoy, D. T. & et al.: Causes of higher climate sensitivity in CMIP6 models. *Geophys. Res. Lett.*, **47**, e2019GL085782, 2020.

https://doi.org/10.5194/egusphere-2024-872
Preprint. Discussion started: 10 April 2024

Tables

Table 1. Description of CESM2/CAM6 methane and carbon dioxide experiments. Both fixed climatological sea surface temperature and coupled ocean atmosphere simulations are performed for each experiment. 2.5x preindustrial atmospheric methane concentrations represent the present-day methane perturbation which corresponds to a ~750 to ~1900 ppb increase (i.e., ~150%). Analogous experiments are conducted for $2xCO_2$ and $4xCO_2$.

Experiment	Description
$2.5xCH_4^{EXP}$	2.5xCH_4 with CH_4 LW+SW radiative effects
$2.5xCH_{4NOSW}^{EXP}$	2.5xCH_4 with CH_4 SW radiative effects turned off
PIC^{EXP}	Preindustrial CH_4 with CH_4 LW+SW radiative effects
$PIC_{NOCH4SW}^{EXP}$	Preindustrial CH_4 with CH_4 SW radiative effects turned off
Signal	**Description**
$2.5xCH_{4LW+SW} = 2.5xCH_4^{EXP} - PIC^{EXP}$	Response to CH_4 LW+SW radiative effects
$2.5xCH_{4LW} = 2.5xCH_{4NOSW}^{EXP} - PIC_{NOCH4SW}^{EXP}$	Response to CH_4 LW radiative effects
$2.5xCH_{4SW} = (2.5xCH_4^{EXP} - PIC^{EXP}) - (2.5xCH_{4NOSW}^{EXP} - PIC_{NOCH4SW}^{EXP})$	Response to CH_4 SW radiative effects

https://doi.org/10.5194/egusphere-2024-872
Preprint. Discussion started: 10 April 2024

Figures

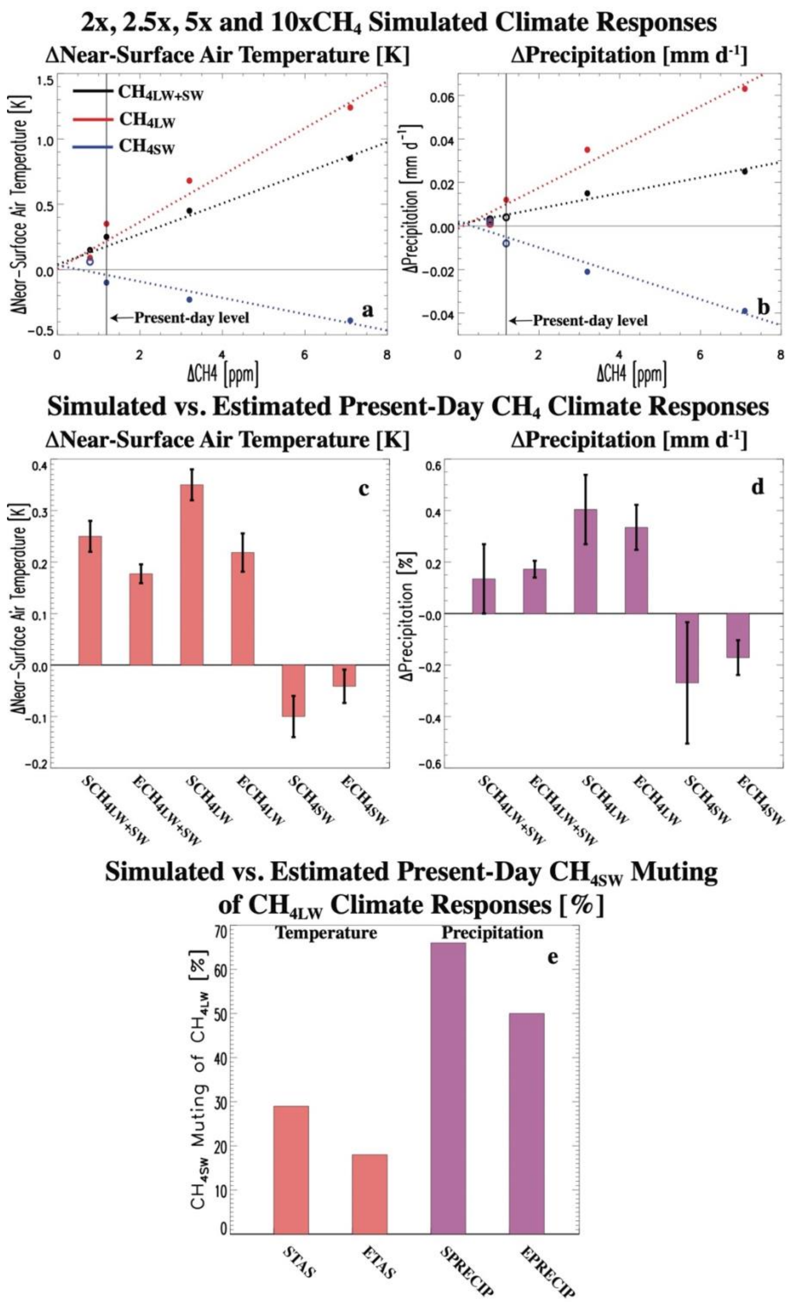

Figure 1. Climate response to methane perturbations. Global annual mean (a) near-surface air temperature [units are K] and (b) precipitation [units are mm d^{-1}] response for 2xCH_4 (0.79 ppm), 2.5xCH_4 (1.19 ppm), 5xCH_4 (3.16 ppm) and

https://doi.org/10.5194/egusphere-2024-872
Preprint. Discussion started: 10 April 2024

$10xCH_4$ (7.11 ppm) from coupled ocean atmosphere simulations. Responses are shown for methane longwave and shortwave radiative effects (CH_{4LW+SW}; black), methane longwave radiative effects (CH_{4LW}; red) and methane shortwave radiative effects (CH_{4SW}; blue). Dotted lines show the least-squares regressions based on the three simulations from A23, including $2xCH_4$, $5xCH_4$ and $10xCH_4$. A significant response at the 90% confidence level, based on a standard t-test, is denoted by solid (as opposed to open) circles. The black vertical line denotes the $2.5xCH_4$ 1.19 ppm perturbation. Also included are the regression-estimated (denoted with an "E") and explicitly simulated (denoted with a "S") present-day CH_4 climate responses for (c) near-surface air temperature [K; pink] and (d) precipitation [%; purple]. The sum of the CH_{4LW} and CH_{4SW} bars is the same as CH_{4LW+SW}. Error bars in (c, d) display the 1-standard deviation uncertainty. For the estimated responses, uncertainty is based on the regression slope, which is estimated from the 2x, 5x and $10xCH_4$ like-colored data points from the simulations in panels (a) and (b). The regression-estimated response is the error-bar center. For the explicitly simulated responses, uncertainty is based on the pooled variance. Panel (e) shows the present-day CH_{4SW} muting of CH_{4LW} [units are %] climate responses for both near-surface air temperature (pink bars) and precipitation (purple bars) based on the regression-estimate (denoted with an "E") and simulation (denoted with an "S").

https://doi.org/10.5194/egusphere-2024-872
Preprint. Discussion started: 10 April 2024

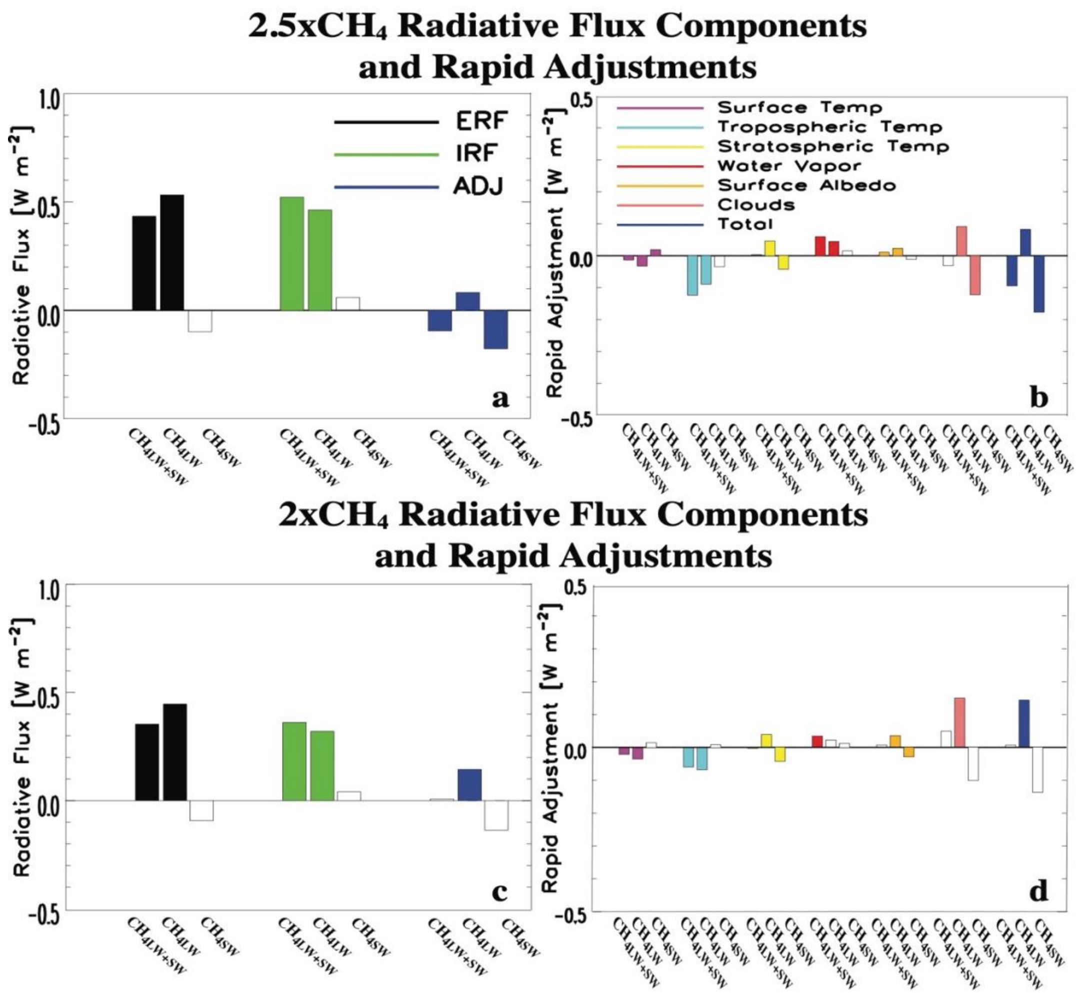

Figure 2. Top-of-the-atmosphere radiative flux components and rapid adjustments for 2.5xCH_4 and 2xCH_4. Global annual mean top-of-the-atmosphere (TOA) (a, c) effective radiative forcing (ERF; black), instantaneous radiative forcing (IRF; green) and rapid adjustment (ADJ; blue); and (b, d) decomposition of the rapid adjustment into its components including surface temperature (purple), tropospheric temperature (cyan), stratospheric temperature (yellow), water vapor (red), surface albedo (orange), cloud (pink) and total rapid adjustment (blue) for (a, b) 2.5xCH_4 and (c, d) 2xCH_4. Responses are decomposed into methane longwave and shortwave radiative effects (CH_{4LW+SW}), methane longwave radiative effects (CH_{4LW}) and methane shortwave radiative effects (CH_{4SW}). ERF and rapid adjustments are based on 30-year fixed climatological sea surface temperature simulations. Unfilled bars denote responses that are not significant at the 90% confidence level. Units are W m^{-2}.

https://doi.org/10.5194/egusphere-2024-872
Preprint. Discussion started: 10 April 2024

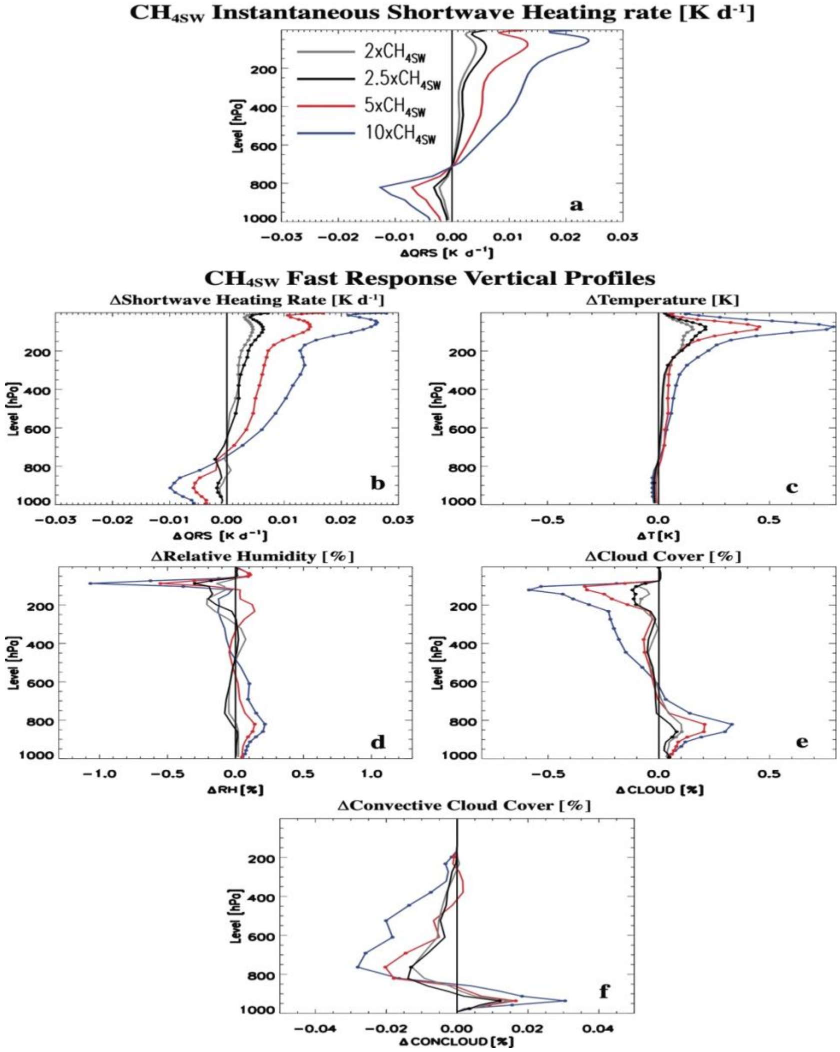

Figure 3. Global mean annual mean vertical response profiles for four CH_{4SW} perturbations. Instantaneous (a) shortwave heating rate (QRS; units are K d^{-1}); and (b-f) fast responses of (b) QRS (units are K d^{-1}); (c) air temperature (T; units are K); (d) relative humidity (RH; units are %); (e) cloud cover (CLOUD; units are %) and (f) convective cloud cover (CONCLOUD; units are %) for 2xCH_{4SW} (gray); 2.5xCH_{4SW} (black); 5xCH_{4SW} (red); and 10xCH_{4SW} (blue). The 2xCH_4, 5xCH_4 and 10xCH_4 simulations are from A23. A significant response at the 90% confidence level, based on a standard t-test, is denoted by solid dots in (b-f). Climatologically fixed SST simulations are used to estimate the fast responses. Instantaneous QRS profiles come from the Parallel Offline Radiative Transfer Model (PORT).

https://doi.org/10.5194/egusphere-2024-872
Preprint. Discussion started: 10 April 2024

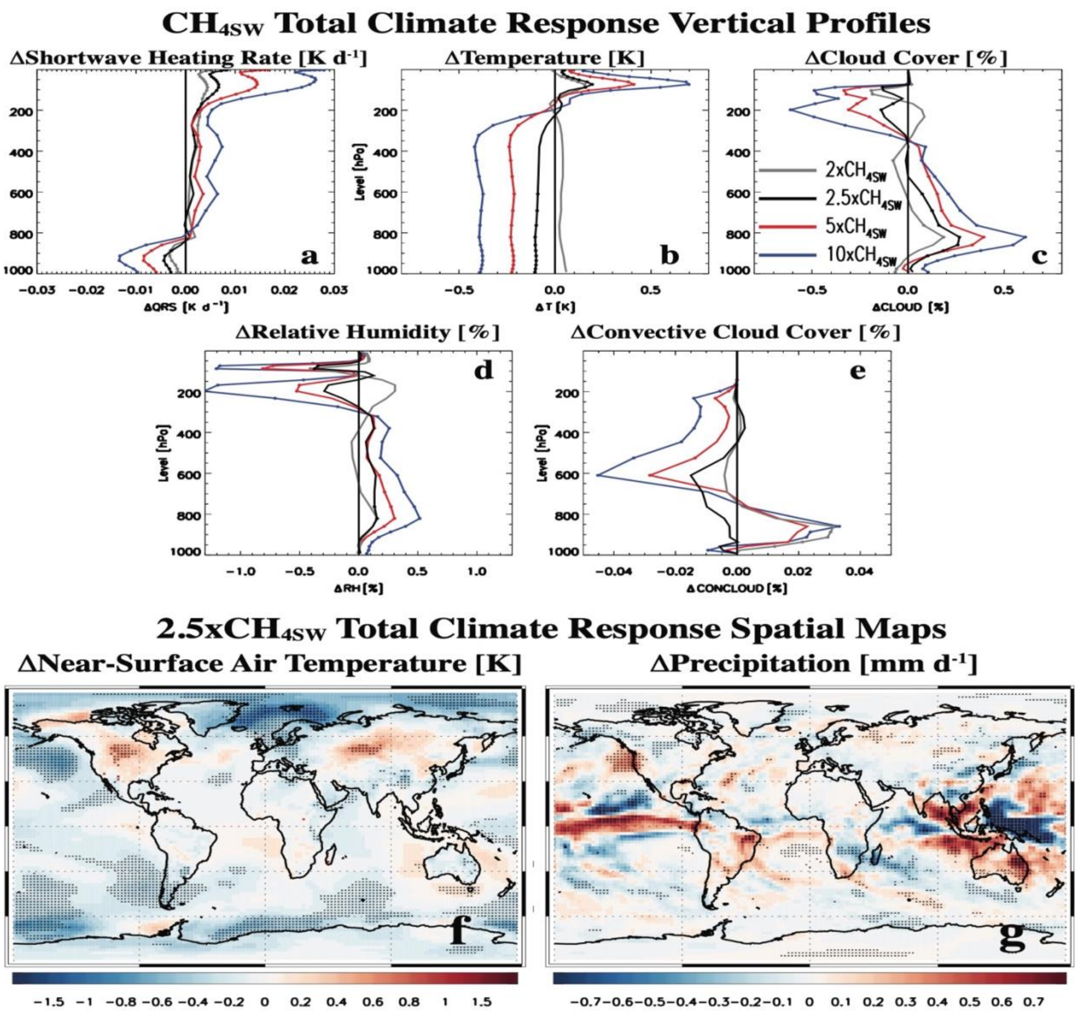

Figure 4. Total climate responses to CH_{4SW}. Annual mean global mean vertical response profiles of (a) shortwave heating rate (QRS; units are K d^{-1}); (b) air temperature (T; units are K); (c) cloud cover (CLOUD; units are %); (d) relative humidity (RH; units are %); and (e) convective cloud cover (CONCLOUD; units are %) for $2xCH_{4SW}$ (gray); $2.5xCH_{4SW}$ (black); $5xCH_{4SW}$ (red); and $10xCH_{4SW}$ (blue). The $2xCH_{4SW}$, $5xCH_{4SW}$ and $10xCH_{4SW}$ simulations are from A23. Also included are global maps of the annual mean (f) near-surface air temperature [K] and (g) precipitation [mm d^{-1}] response for $2.5xCH_{4SW}$. A significant response at the 90% confidence level, based on a standard t-test, is denoted by solid dots. Climate responses are estimated from coupled ocean-atmosphere CESM2 simulations.

https://doi.org/10.5194/egusphere-2024-872
Preprint. Discussion started: 10 April 2024

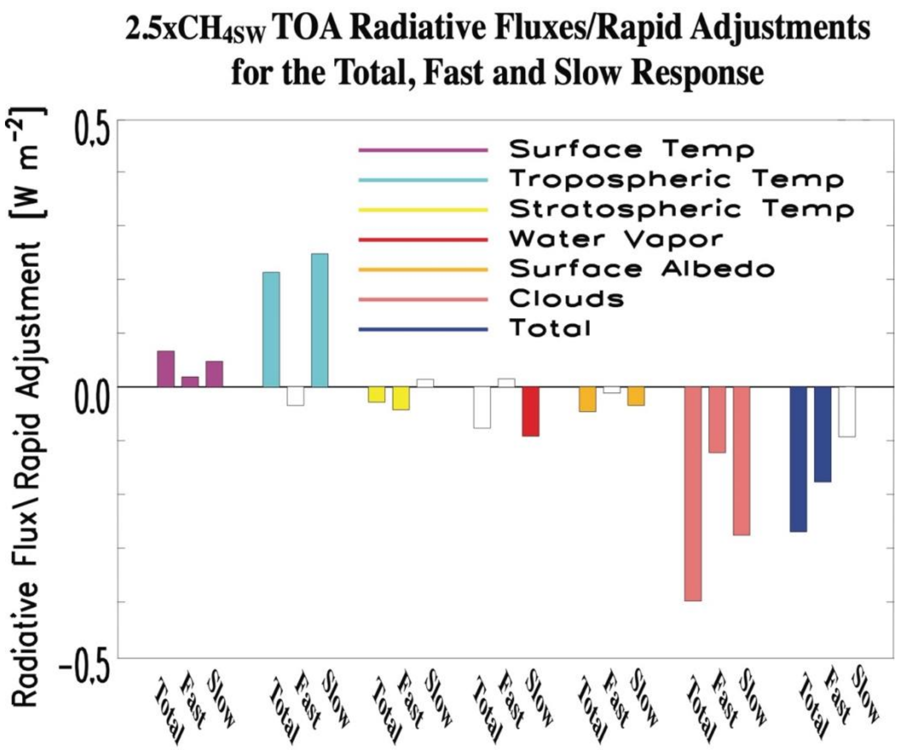

Figure 5. 2.5xCH$_{4SW}$ top-of-the-atmosphere radiative flux decomposition for the total response, ADJ and feedback. Global annual mean top-of-the-atmosphere (TOA) surface temperature (purple), tropospheric temperature (cyan), stratospheric temperature (yellow), water vapor (red), surface albedo (orange), cloud (pink) and total (blue) radiative flux decomposition for 2.5xCH$_{4SW}$. The total response (from the coupled ocean atmosphere simulations) is represented by the first bar in each like-colored set of three bars; the rapid adjustment (fast response from fixed climatological sea surface temperature simulations) is represented by the second bar; and the surface-temperature-induced feedback (slow response; estimated as the difference of the total response minus the fast response) is represented by the third bar. Unfilled bars denote responses that are not significant at the 90% confidence level. Units are W m^{-2}.

https://doi.org/10.5194/egusphere-2024-872
Preprint. Discussion started: 10 April 2024

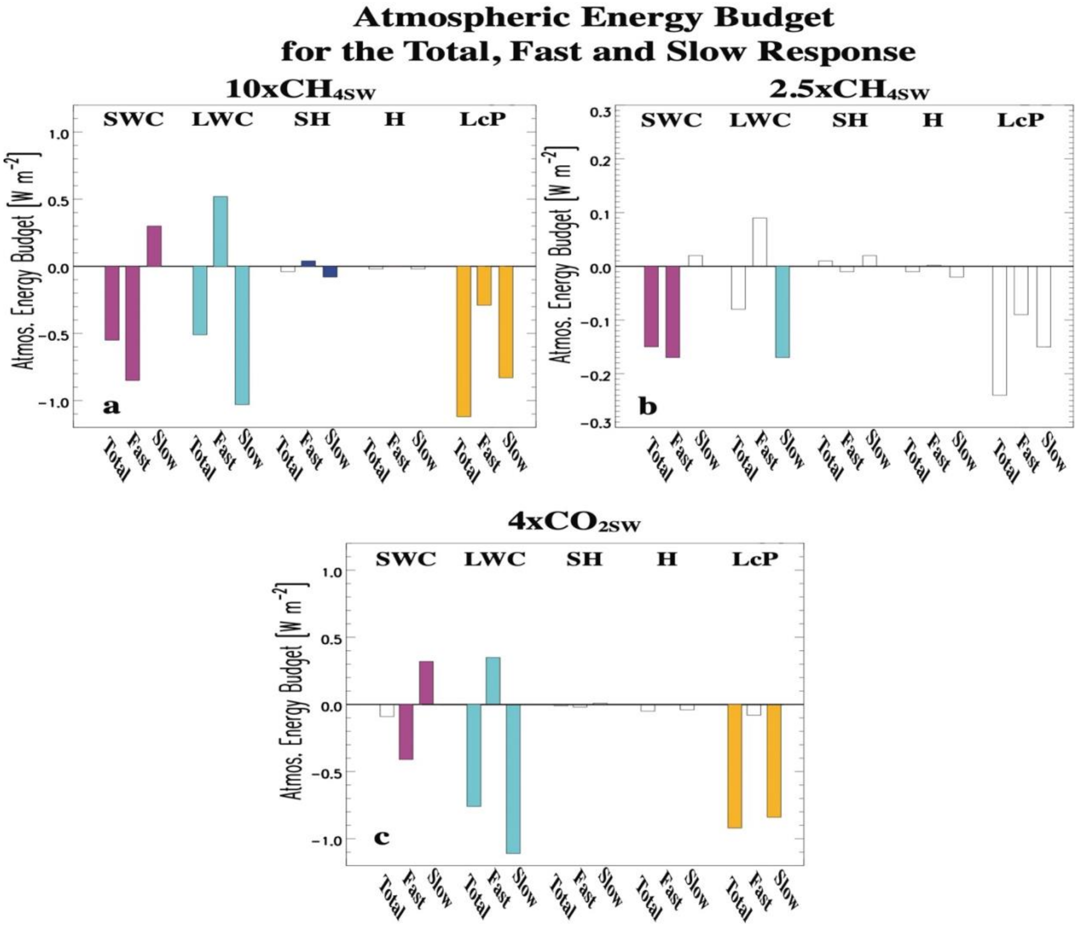

Figure 6. Atmospheric energy budget decomposition for the total, fast and slow response. Annual mean global mean energy budget decomposition for (a) $10xCH_{4SW}$; (b) $2.5xCH_{4SW}$ and (c) $4xCO_{2SW}$. Components include net shortwave radiative cooling from the atmospheric column (SWC); net longwave radiative cooling from the atmospheric column (LWC); net downwards sensible heat flux at the surface (SH); column integrated dry static energy flux divergence (H); and total latent heating (L_cP). The sum of the first four terms is equal to the last term (L_cP). The total response (from the coupled ocean atmosphere simulations) is represented by the first bar in each like-colored set of three bars; the rapid adjustment (fast response from fixed climatological sea surface temperature simulations) is represented by the second bar; and the surface-temperature-induced feedback (slow response; estimated as the difference of the total response minus the fast response) is represented by the third bar. Unfilled bars denote responses that are not significant at the 90% confidence level. Units are W m^{-2}. Note the different y-axis in panel b.

https://doi.org/10.5194/egusphere-2024-872
Preprint. Discussion started: 10 April 2024

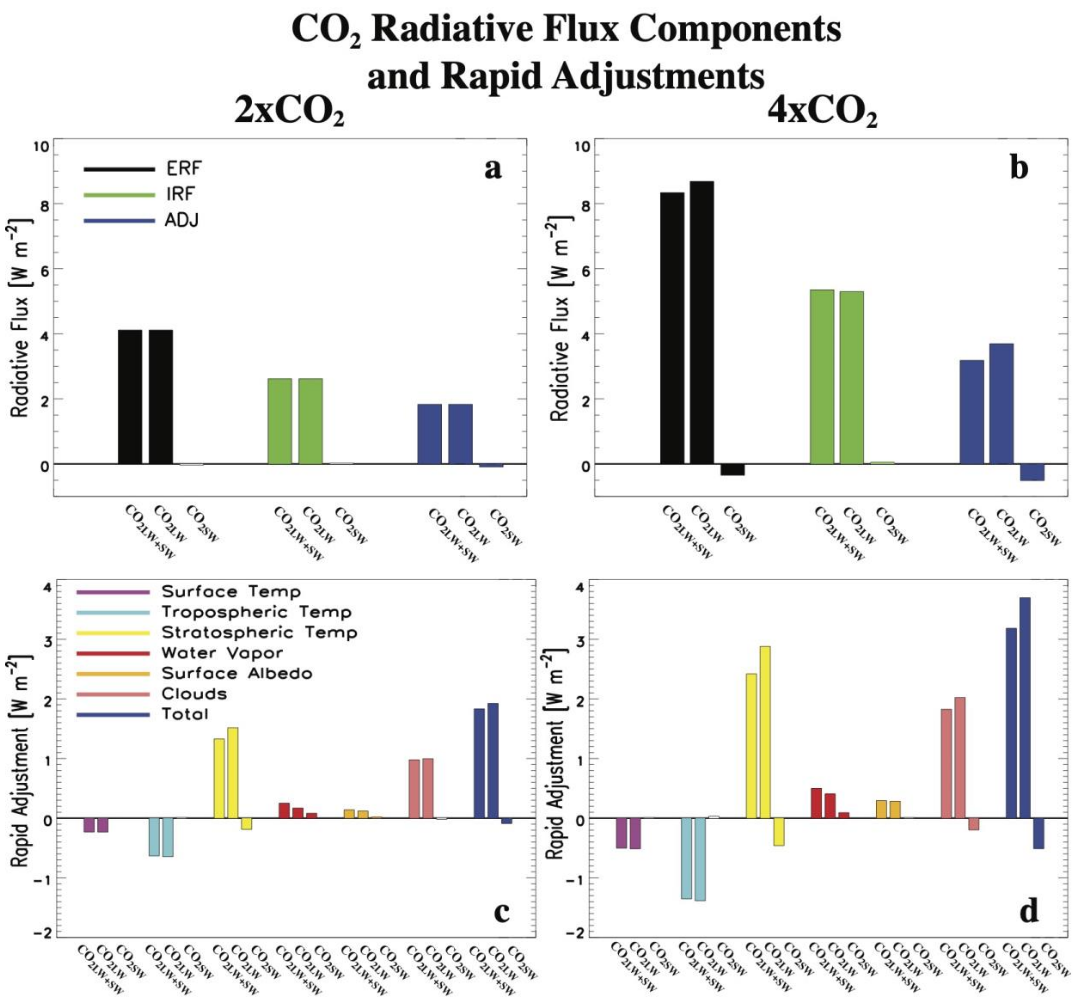

Figure 7. 2xCO_2 and 4xCO_2 top-of-the-atmosphere radiative flux components and rapid adjustments. Global annual mean TOA (a, b) effective radiative forcing (ERF; black), instantaneous radiative forcing (IRF; green) and rapid adjustment (ADJ; blue); and (c, d) decomposition of the rapid adjustment into its components including surface temperature (purple), tropospheric temperature (cyan), stratospheric temperature (yellow), water vapor (red), surface albedo (orange), cloud (pink) and total rapid adjustment (blue) for (a, c) 2xCO_2 and (b, d) 4xCO_2. Responses are decomposed into CO_2 longwave and shortwave radiative effects (CO_{2LW+SW}), CO_2 longwave radiative effects (CO_{2LW}) and CO_2 shortwave radiative effects (CO_{2SW}). ERF and rapid adjustments are based on 30-year fixed climatological sea surface temperature simulations. Unfilled bars denote responses that are not significant at the 90% confidence level. Units are W m^{-2}.

https://doi.org/10.5194/egusphere-2024-872
Preprint. Discussion started: 10 April 2024

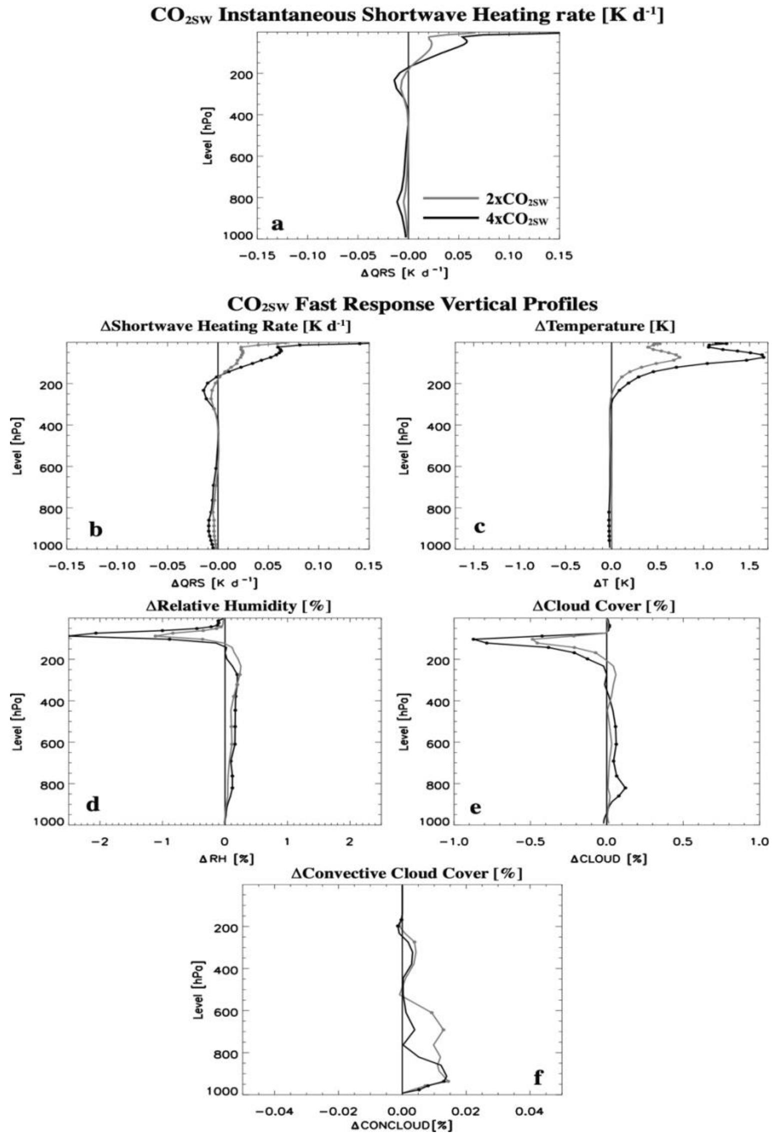

Figure 8. Global mean annual mean vertical response profiles for two CO_{2SW} perturbations. Instantaneous (a) shortwave heating rate (QRS; units are K d^{-1}); and (b-f) fast responses of (b) QRS (units are K d^{-1}); (c) air temperature (T; units are K); (d) relative humidity (RH; units are %); (e) cloud cover (CLOUD; units are %) and (f) convective cloud cover (CONCLOUD; units are %) for $2xCO_{2SW}$ (gray); and $4xCO_{2SW}$ (black). A significant response at the 90% confidence level, based on a standard t-test, is denoted by solid dots in (b-f). Climatologically fixed SST simulations are used to estimate the fast responses. Instantaneous QRS profiles come from the Parallel Offline Radiative Transfer Model (PORT).

https://doi.org/10.5194/egusphere-2024-872
Preprint. Discussion started: 10 April 2024

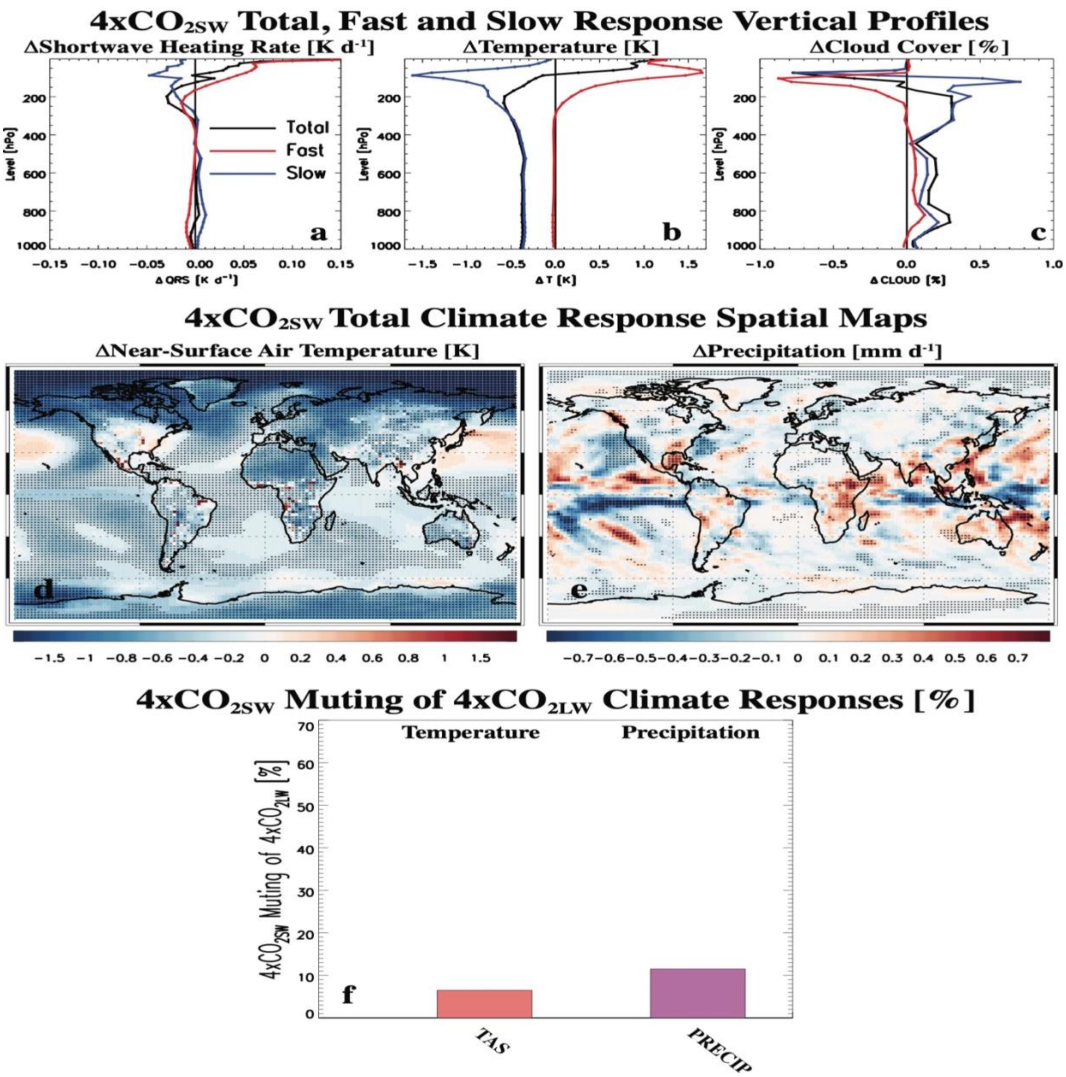

Figure 9. 4xCO_{2SW} responses. 4xCO_{2SW} annual mean global mean vertical response profiles of (a) shortwave heating rate (QRS; units are K d^{-1}); (b) air temperature (T; units are K); and (c) cloud cover (CLOUD; units are %) for the total (black); fast (red) and slow (blue) response. Also included are 4xCO_{2SW} global maps of the annual mean (d) near-surface air temperature [K] and (e) precipitation [mm d^{-1}] change for the total climate response. A significant response at the 90% confidence level, based on a standard t-test, is denoted by solid dots. Panel (f) shows the 4xCO_{2SW} muting of 4xCO_{2LW} [units are %] total climate response for both near-surface air temperature (pink bars) and precipitation (purple bars). Total climate responses are estimated using from coupled ocean-atmosphere CESM2 simulations.

https://doi.org/10.5194/egusphere-2024-872
Preprint. Discussion started: 10 April 2024

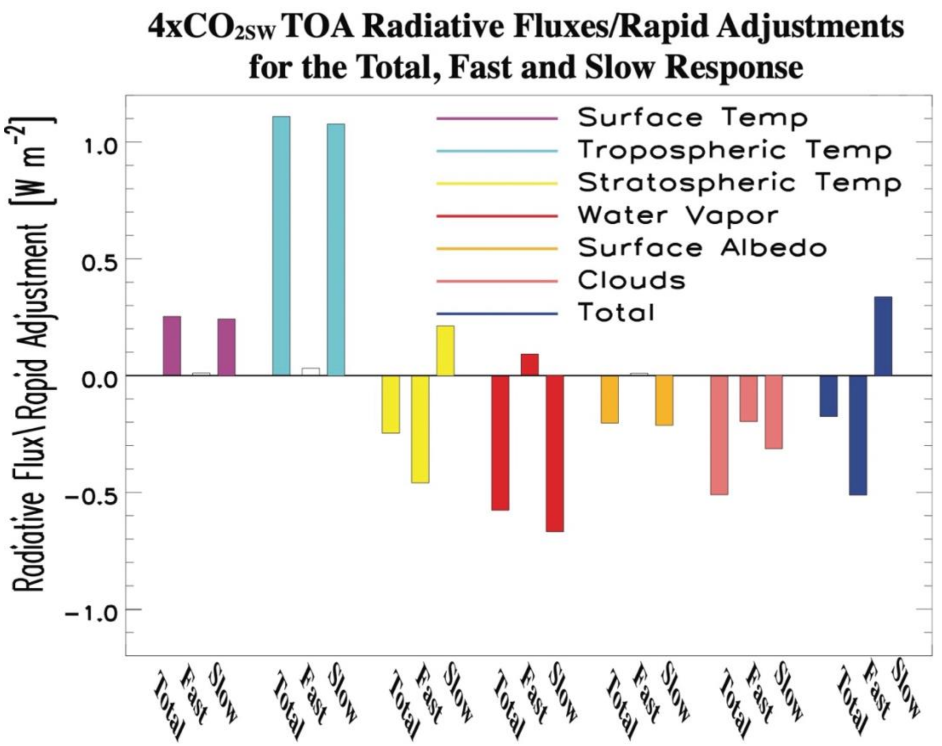

Figure 10. 4xCO_{2SW} top-of-the-atmosphere radiative flux decomposition for the total response, ADJ and feedback. Global annual mean top-of-the-atmosphere (TOA) surface temperature (purple), tropospheric temperature (cyan), stratospheric temperature (yellow), water vapor (red), surface albedo (orange), cloud (pink) and total (blue) radiative flux decomposition for 4xCO_{2SW}. The total response (from the coupled ocean atmosphere simulations) is represented by the first bar in each like-colored set of three bars; the rapid adjustment (fast response from fixed climatological sea surface temperature simulations) is represented by the second bar; and the surface-temperature-induced feedback (slow response; estimated as the difference of the total response minus the fast response) is represented by the third bar. Unfilled bars denote responses that are not significant at the 90% confidence level. Units are W m^{-2}.